

1 **Spatio-temporal variations in surface Marine Carbonate**  
2 **System properties across the Western Mediterranean Sea**  
3 **using Volunteer Observing Ship data.**

4 David Curbelo-Hernández\*, David González-Santana, Aridane González-González, J.  
5 Magdalena Santana-Casiano and Melchor González-Dávila

6 <sup>1</sup> Instituto de Oceanografía y Cambio Global (IOCAG), Universidad de Las Palmas de  
7 Gran Canaria (ULPGC). Las Palmas de Gran Canaria, Spain.

8 \* Corresponding Author: david.curbelo@ulpgc.es

## 9 Abstract

10 The surface physical and Marine Carbonate System (MCS) properties were assessed  
11 along the western boundary of the Mediterranean Sea. An unprecedented high-resolution  
12 observation-based dataset spanning 5 years (2019-2024) was built through automatically  
13 underway monitoring by a Volunteer Observing Ship (VOS). The MCS dynamics were  
14 strongly modulated by physical-biological coupling dependent on the upper-layer  
15 circulation and mesoscale features. The variations in CO<sub>2</sub> fugacity ( $f\text{CO}_{2,\text{sw}}$ ) were mainly  
16 driven by sea surface temperature (SST) changes. On a seasonal scale, SST explained 51-  
17 71% of the increase in  $f\text{CO}_{2,\text{sw}}$  from February to September, while total alkalinity ( $A_T$ )  
18 and sea surface salinity (SSS) explained <20%. The processes controlling total inorganic  
19 carbon ( $C_T$ ) partially offset this increment and explained ~23-37% of the  $f\text{CO}_{2,\text{sw}}$  seasonal  
20 change. On an interannual scale, the SST trends (0.26-0.43 °C yr<sup>-1</sup>) have accelerated by  
21 78-88% in comparison with previous decades. The ongoing surface warming contributed  
22 by ~76-92% in increasing  $f\text{CO}_{2,\text{sw}}$  (4.18 to 5.53 μatm yr<sup>-1</sup>) and, consequently, decreasing  
23 pH (-0.005 to -0.007 units yr<sup>-1</sup>) in the surface waters. The seasonal amplitude of SST,  
24 becoming larger due to progressively warmer summers, was the primary driver of the  
25 observed slope up of interannual trends. The evaluation of the air-sea CO<sub>2</sub> exchange  
26 shows the area across the Alboran Sea (14,000 Km<sup>2</sup>) and the eastern Iberian margin  
27 (40,000 Km<sup>2</sup>) acting as an atmospheric CO<sub>2</sub> sink of  $-1.57 \pm 0.49 \text{ mol m}^{-2} \text{ yr}^{-1}$  ( $-0.97 \pm 0.30$   
28 Tg CO<sub>2</sub> yr<sup>-1</sup>) and  $-0.70 \pm 0.54 \text{ mol m}^{-2} \text{ yr}^{-1}$  ( $-1.22 \pm 0.95 \text{ Tg CO}_2 \text{ yr}^{-1}$ ), respectively.  
29 Considering the spatial variability of CO<sub>2</sub> fluxes across the study area, a reduction of  
30 approximately 40–80% in the net annual CO<sub>2</sub> sink is estimated since 2019, which is  
31 attributed to the persistent strengthening of the source status during summer and the  
32 weakening of the sink status during spring and autumn.

33 **Keywords:** Marine Carbonate System, Air-sea CO<sub>2</sub> fluxes, Volunteer Observing Ships,  
34 Western Mediterranean Sea, ocean acidification, sea-surface warming

## 1. Introduction

The semi-enclosed and marginal seas have a relevant role in the global biogeochemical cycles and are highly vulnerable to climate change (IPCC, 2023). These regions accomplish extensive coastal and continental shelf and slope areas occupied with multiple diverse ecosystems under anthropogenic pressure. Although these regions present enhanced biogeochemical activity and intensified air-sea CO<sub>2</sub> exchange rates compared to the open ocean (Borges et al., 2005; Cai et al., 2006; Frankignoulle and Borges, 2001; Shadwick et al., 2010), its poorly monitoring and assessment have historically excluded them from global studies and models and underestimated in the Global Carbon Budget (Friedlingstein et al., 2023)

The Mediterranean Sea is a dynamic semi-enclosed system potentially fragile to natural and anthropogenic forcing (e. g. Álvarez et al., 2014; Tanhua et al., 2013). The particular oceanography of the Mediterranean Sea, collectively described in several works (e.g. Nielsen, 1912; Robinson et al., 2001; Millot and Taupier-Letage, 2005; Bergamasco and Malanotte-Rizzoli, 2010; Schroeder et al., 2012), have rendered it a “miniature ocean” considered as “laboratory basin” to evaluate physico-chemical perturbations that can be extrapolated to larger scales in the global ocean (e.g. Robinson and Golnaraghi, 1994; Bergamasco and Malanotte-Rizzoli, 2010). These perturbations have accelerated since the second half of the 20<sup>th</sup> century, with temperature and salinity increasing at unprecedented rates of 0.04°C and 0.015 per decade, respectively (Borghini et al., 2014), impacting the Marine Carbonate System (MCS). However, the availability of high-quality observation-based data and research in this basin is scarce due to spatial and temporal limitations in the monitoring and sampling techniques (Millero et al., 1979; Rivaro et al., 2010).

The MCS dynamics has been evaluated in the Northwestern Mediterranean basin (Bégovic and Copin-Montégut, 2002; Copin-Montégut and Bégovic, 2002, 2004; Coppola et al., 2020; Hood and Merlivat, 2001; Mémery et al., 2002; Merlivat et al., 2018; Touratier and Goyet, 2009; Ulses et al., 2023), mainly conducted at the time-series DYFAMED (43.42 °N, 7.87 °E; Marty, 2002) and BOUSSOLE sites (43.37° N, 7.90° E; Antoine et al., 2006, 2008a, 2008b). These investigations have shown the seasonal cycle of the surface CO<sub>2</sub> is primarily governed by thermal fluctuations and the behaviour of the area as a relatively weak sink for atmospheric CO<sub>2</sub> on an annual scale. Long-term changes

estimated by Merlivat et al., (2018) reported the increase in the surface CO<sub>2</sub> fugacity ( $f\text{CO}_{2,\text{sw}}$ ) and pH of  $\sim 40 \mu\text{atm}$  and  $\sim 0.04$  units, respectively, since the 90s decade. The interannual trends given for  $f\text{CO}_{2,\text{sw}}$  ( $2.3 \pm 0.23 \mu\text{atm yr}^{-1}$ ; Merlivat et al., 2018) and pH ( $0.002\text{--}0.003 \text{ units yr}^{-1}$ ; Yao et al., 2016) were in agreement with those encountered in the Northeast Atlantic at the ESTOC site ( $2.1 \pm 0.1 \mu\text{atm yr}^{-1}$  and  $0.002 \pm 0.0001 \text{ units yr}^{-1}$ , respectively; González-Dávila and Santana-Casiano, 2023). Long-term variations in MCS within the northwestern Mediterranean occur at rates exceeding those anticipated from chemical equilibrium with atmospheric CO<sub>2</sub>, which has been attributed to the intense deep-convection processes in this area (Copin-Montégut, 1993; D’Ortenzio et al., 2008; Cossarini et al., 2021) and the substantial input of anthropogenic carbon from the North Atlantic (Merlivat et al., 2018; Palmiéri et al., 2015; Schneider et al., 2010; Ulses et al., 2023). Based on a high-resolution regional model, Palmiéri et al., (2015) estimated that  $\sim 25\%$  of the anthropogenic carbon storage in the Mediterranean Sea comes from the Atlantic. The water exchange processes in the Strait of Gibraltar become the western boundary of the Mediterranean Sea in a crucial region for MCS variability which significantly modulates the basin-wide anthropogenic carbon inventory and ocean acidification trends in the Mediterranean basin and could affect significantly the general circulation and the composition of seawaters in the North Atlantic. Additionally, this region is subject to variability related with (1) the intense deep-water convection in the adjacent Northwestern area of the Mediterranean Sea and (2) the unique circulation patterns shaped to the irregular coastlines and islands, which forms quasi-permanent eddies and other (sub)mesoscale features (Alberola et al., 1995; Bosse et al., 2021; 2016; Bourg and Molcard, 2021).

This research focus on the surface spatio-temporal variations of the MCS and air-sea CO<sub>2</sub> fluxes in the western boundary of the Mediterranean Sea. High-resolution and reliable data were obtained through autonomous underway monitoring of the surface ocean from February 2019 to February 2024 by a Volunteer Observing Ship (VOS). This systematic strategy represents a powerful tool to analyse the distribution and changes of physical and MCS properties in highly variable areas as coastal transitional zones where the availability of data has been historically scarce. The cruise track (Figure 1) followed the south and east geographically rugged coastline of the Iberian Peninsula and allowed the characterization of the Alboran Sea ( $\sim 2\text{--}5.1^\circ\text{W}$ ) separately from the eastern coastal and shelf area between Cape of Gata (Almería) and Barcelona ( $\sim 36.5\text{--}41.3^\circ\text{N}$ ). The changes

observed in the MCS on a seasonal and interannual timescales (even considering the limitations of 5 years of data), the mechanism controlling their variations and the changes in the air-sea CO<sub>2</sub> exchange have been attended in this study.

## **2. Material and methods**

### **2.1. Study area**

The Western boundary of the Mediterranean Sea encompasses the Alboran Sea, land-loaded by the southern Iberian Peninsula coast and northern African coast, and the coastal transitional area along the eastern Iberian margin (Figure 1a). The classical surface circulation pattern in the Alboran Sea (e. g. Bormans and Garrett, 1989; Peliz et al., 2013; Sánchez-Garrido et al., 2013, 2022; Speich, 1996; Whitehead and Miller, 1979), with the Atlantic water jet (AJ) following wavelike path of the quasi-permanent Western Anticyclonic Gyre (WAG) and the Eastern Anticyclonic Gyre (EAG) and constituting the Modified Atlantic Water (MAW; Lopez-García et al., 1994; Viúdez et al., 1998), drive west-to-east variations in physical and biogeochemical terms. The intensity and direction of the AJ, depending primarily on sea level pressure and local wind fluctuations, variate on different timescales and govern the circulation patterns in the Alboran Sea influencing the biogeochemistry (Sánchez-Garrido and Nadal, 2022; Solé et al., 2016). On a seasonal scale, the AJ oscillate between two main circulation modes (García-Lafuente et al., 2002; Macías et al., 2008, 2016; Vargas-Yáez et al., 2002), detectable by reanalysis data-based SST signals (Figure 1b): a high-intense AJ flowing north-eastward during spring/summer and a lower-intense AJ flowing with more south-eastwardly direction during autumn/winter. The stronger AJ during the warm months feed the classical two-gyres configuration in the Alboran Sea, while the weak AJ only allows the existence of the WAG (Renault et al., 2012). The AJ forms a filament flowing from the Iberian coastal upwelling in the northwestern Alboran Sea and surrounding the eastern edge of the WAG, which is most frequently presented during summer (Gómez-jakobsen et al., 2019; Millot, 1999). The westernmost part of the Alboran Sea is affected by the shallow position of the Atlantic-Meridional Interface layer (AMI; Bray et al., 1995; Lacombe and Richez, 1982), which promotes the injection of deep-water into the surface (Echevarría et al., 2002; Gómez-jakobsen et al., 2019; Minas et al., 1991).

The eastern Iberian margin is influenced by the path of the Northern Current transporting Mediterranean Water (MW; Pinot et al., 1995), which is originated around the Gulf of

Lion where the forcing of the northeasterly winds is frequently strong and flows southward along the eastern coastline of the Iberian Peninsula (Conan and Millot, 1995; Millot, 1999; Sammari et al., 1995). The seasonality of the Northern Current (Millot, 1999) infers meridional variations in the thermal signals between cold and warm months (Figure 1b). The enhanced wind-forcing during winter intensify the Northern Current, which fit to the Iberian continental slope and recirculate offshore at Cape of Nao (Millot, 1999), while a low-intense branch progress southward Cape of Nao and reach the eastern Alboran Sea. During summer, the weakening in the wind-forcing forms a surface thermal front in the axis of the Pyrenees, which was detectable in the reanalysis-based SST map (Figure 1b). This front changes the path of the Northern Current further away from the Iberian coast (Lopez-García et al., 1994), which allow the MAW to reach its northern most spreading. The interaction of the Northern Current with the variety of mesoscale features (mainly meanders and eddies) and the variations in stratification within the annual cycle introduced spatio-temporal differences in the biogeochemical properties (Bosse et al., 2021; Millot, 1999). Additionally, although terrestrial and riverine inputs have a less pronounced impact on biogeochemistry compared to the eastern Mediterranean basin (Cossarini et al., 2015), they can act as a source of local variability. The most significant in this area is the Ebro river runoff, which peaks in March-May due to the combined action of precipitation during winter and snowmelt in the upper river basins during spring (Zambrano-Bigiarini et al., 2010). It feed the coastal area around the Ebro Delta with fresh and cool waters (see in minimum SST compared to adjacent waters in February; Figure 1b).

## **2.2. Data collection**

A high spatio-temporal resolution dataset spanning 5 years was constructed based on weekly physico-chemical observations of the surface western boundary of the Mediterranean Sea between February 2019 and February 2024. Data was automatically collected by the Volunteer Observing Ship (VOS) MV JONA SOPHIE (IMO: 9144718, called RENATE P before November 2021), a container ship managed in Spain by Nisa Maritima which links the Canary Islands with Barcelona. This VOS line was designed and is maintained by the QUIMA research group at the IOCAG-ULPGC, and operates within the framework of the Integrated Carbon Observation System (ICOS; <https://www.icos-cp.eu/>; last assess: 15 May 2025) as a Ship-of-Opportunity (SOOP) Ocean Station (Station ID: ES-SOOP-CanOA) since 2021 (upgraded to an ICOS Class 1

Ocean Station in May, 2024). Therefore, the measurement equipment and underway data collection techniques verify the ICOS high-quality requirements and methodological recommendations.

The ES-SOOP-CanOA station allows the monitoring of a coastal transitional zone transect across the western Mediterranean Sea (Figure 1), together with a northeast Atlantic subtropical area (Curbelo-Hernández et al., 2021a) and the Strait of Gibraltar (Curbelo-Hernández et al., 2021b). In the Alboran Sea, the vessel advanced eastward and longitudinally crossed the WAG through its northern part and followed the northern path of the EAG. The irregular southeast and east coastline of the Iberian Peninsula caused local differences in the oceanographic features and variances in the distance-to-land of the vessel track.

The system operates fully unattended in underway mode, with biweekly (time required to complete a round trip) routine maintenance at the port of Las Palmas de Gran Canaria (28.13 °N, 15.42 °W). Data is automatically transferred to a server when the vessel docks at each of the port along the usual route (Las Palmas de Gran Canaria, Santa Cruz de Tenerife, Arrecife, Sagunto and Barcelona). A total of 92 routes were completed in the Mediterranean Sea (Figure 1).

### **2.3.Monitoring routines**

The autonomous underway monitoring of CO<sub>2</sub> in surface ocean (water intake placed at 5 m depth) and low atmosphere (air intake placed at 8 m above sea level) and the data collection routines followed the recommendations described by Pierrot et al., (2009) to ensure comparable and high-quality datasets. An automated underway CO<sub>2</sub> molar fraction (xCO<sub>2</sub>, ppm) measurement system, developed by Craig Nail and commercialized by General Oceanics™, was installed inside the engine room of the vessel and described by Curbelo et al. (2021a, 2021b).

The xCO<sub>2</sub> measurement system combines an air and seawater equilibrator, placed inside the wet box, with a non-dispersive infrared analyser for gas detection, placed inside the dry box. The analyser used for xCO<sub>2</sub> detection was built by LICOR® (initially LI-6262 model and after October 2019, LI-7000 model). The nominal accuracy of the LICOR infrared gas analyser given by the manufacturer is 1% for CO<sub>2</sub> concentrations within the range of 0 to 3000 ppm. The system performs in-loop, at 3-minute intervals, five

measurements of atmospheric  $x\text{CO}_2$  ( $x\text{CO}_{2,\text{atm}}$ ) and eighty measurements of surface seawater  $x\text{CO}_2$  ( $x\text{CO}_{2,\text{sw}}$ ). The  $x\text{CO}_{2,\text{atm}}$  data was consistent with daily  $x\text{CO}_{2,\text{atm}}$  records from the Izaña Atmospheric Research Center (IZO site located in Tenerife, Canary Islands, Spain; 28.3090°N, 16.499°W, placed at 2372.9 m above sea level; <https://gml.noaa.gov/dv/site/site.php?code=IZO>, last access: 14 May 2025), which is operated by the Spanish Meteorological Agency (AEMET) and forms part of several major international atmospheric monitoring networks (Figure Sup1). Daily  $x\text{CO}_{2,\text{atm}}$  data from IZO are available through the National Ocean and Atmospheric Administration (NOAA) Global Monitoring Laboratory (GML) dataset (<https://gml.noaa.gov/data/dataset.php?item=izo-co2-flask>; last access: 14 May 2025). During 2019-2024,  $x\text{CO}_{2,\text{atm}}$  measurements from ES-SOOP-CanOA station were, on average, 1.14 ppm higher than those recorded at IZO (Figure Sup1), which may be attributed to the fact that air sampling at IZO is conducted at approximately 2400 meters above sea level, in a remote location far from major urban or industrial areas and above the atmospheric inversion layer, which shields the station from surface-level pollution. In contrast, the ES-SOOP-CanOA measurements are conducted in the lower atmosphere, near the sea surface and closer to greenhouse gas emission sources (particularly when the vessel operates near the coast in the Mediterranean basin).

The LICOR® analyser is automatically calibrated on departure and arrival at each port and periodically every three hours using four standard gases. Additionally, the system is zeroed and spanned (with standard gases 1 and 4, respectively) every twelve hours to properly interpolate the standard values and correct for instrument drift. The four standard gases, with an accuracy of  $\pm 0.02$  ppm, were provided by the NOAA and traceable to the World Meteorological Organization (WMO). They were in the order of 0 ppm, 250 ppm, 400 ppm and 550 ppm until January 2021, when the gas bottles for standard 2 to 4 were changed for a new set with concentrations in the order of 300 ppm, 500 ppm and 800 ppm provided by the ICOS central analytical laboratories.

The sea surface temperature (SST, in °C) was monitored by using a SBE38 thermometer placed at the primary seawater intake in the engine room, with a reported instrumental error of  $\pm 0.01^\circ\text{C}$ . The high sensitivity of  $x\text{CO}_2$  to temperature fluctuations required the monitoring of temperature at different locations across the system. A SBE45 thermosalinograph and a Hart Scientific HT1523 Handheld Thermometer, with reported instrumental errors of  $\pm 0.01^\circ\text{C}$ , were used to monitor the seawater temperature at the



entrance of the wet box and inside the equilibrator, respectively. The measured SST was analysed in conjunction with SST reanalysis monthly data ( $0.042^\circ \times 0.042^\circ$ ; with dates spanning 24 years within 01/01/2000 and 01/03/2024) from the Med MFC physical multiyear product (Escudier et al., 2020; 2021; Nigam et al., 2021), available at Copernicus Marine Data Store (<https://data.marine.copernicus.eu/products>; last access: 15 May 2025). The SST reanalysis data was interpolated to the coordinates of the ES-SOOP-CanOA data to perform direct comparison in their dynamics.

The Sea Surface Salinity (SSS) was measured by the SBE45 thermosalinograph, whose instrumental error fall in the order of  $\pm 0.005$ . Lastly, pressure is measured within  $\pm 0.0002$  atm at the deck box transducer close to the air intake (used as atmospheric pressure), in the wet box inside the equilibrator at the time of equilibration and in the dry box to be used by the LICOR analyser to correct the analog signal for any pressure effects.

Discrete surface seawater samples were manually collected with in situ records of SST and SSS during three round trips in February 2020, March 2021 and October 2023 (a total of 102 were collected in the Mediterranean Sea). The discrete sampling was performed along the vessel track from the seawater supply line every 1-2 hours in borosilicate glass bottles, overfilled and preserved with 100  $\mu\text{l}$  of saturated  $\text{HgCl}_2$ . Samples were kept in dark and analysed just after arriving at port, in a period less than 2 weeks, for total alkalinity ( $A_T$ ,  $\mu\text{mol kg}^{-1}$ ).

The underway observational dataset exhibits a gap of a year between September 2021 and 2022 due to the temporary cessation of the measurement system for vessel maintenance in dry dock. During this period, the measurement system was sent for calibration and maintenance to General Oceanics enterprise, Miami, USA. There are also several gaps of less than a month related with different technical issues with the measurement equipment, which were addressed during the routine maintenance visits to the vessel (i. e. problems with the pump and seawater intake, with the LICOR analyser, depletion of gas bottles supplies, electrical issues in the engine room). Certain technical issues encountered during 2020 were delayed in being resolved due to the constraints imposed by COVID-19.

## **2.4. Calculation procedures**

### **2.4.1. $\text{CO}_2$ system variables**

#### 2.4.1.1. Data processing for $f\text{CO}_2$ calculations

The present investigation followed the data collection methodology, quality control and calculation procedures as published in the updated version of the DOE method manual for ocean  $\text{CO}_2$  analysis (Dickson et al., 2007). The correction of the measured  $x\text{CO}_2$  and calculation of the fugacity of  $\text{CO}_2$  ( $f\text{CO}_2$ ) in surface seawater ( $f\text{CO}_{2,\text{sw}}$ ) and atmosphere ( $f\text{CO}_{2,\text{atm}}$ ) followed the procedure described by Pierrot et al. (2009). This procedure avoids significant uncertainties in the determination of  $f\text{CO}_2$  arising from differences in pressure and temperature conditions between sampling (atmospheric pressure and SST) and equilibration (pressure and seawater temperature inside the equilibrator once equilibration is reached). By calibrating the instrument with standard gases ranging from 0 to 800 ppm (which encompasses the measurement range of 300 to 600 ppm) and actively minimizing temperature and pressure drift through continuous monitoring (see Section 2.3 for standard gas, temperature, and pressure accuracies), the system achieved the target accuracy of  $\pm 0.2 \mu\text{atm}$  for  $f\text{CO}_{2,\text{atm}}$  and  $\pm 2 \mu\text{atm}$  for  $f\text{CO}_{2,\text{sw}}$  (Pierrot et al. 2009). The full set of standard gases was linearly interpolated to the time of observations to generate the calibration curve used for  $x\text{CO}_2$  correction before calculating  $f\text{CO}_2$ .

The raw output data was initially filtered removing data affected by the automatic sampler such as samples measured at low water rates ( $< 2.0 \text{ L min}^{-1}$ ) and/or samples in which the difference in temperature between the seawater intake and the equilibrator was higher than  $1.5^\circ\text{C}$ . The outliers, assumed as elements more than three local standard deviations from the local mean over a window length of fifty elements, were also removed from the dataset. The  $x\text{CO}_2$  measured values in low atmosphere after each calibration were averaged and interpolated at the times of each  $x\text{CO}_2$  observation in seawater by applying a piecewise polynomial-based smoothing spline.

#### 2.4.1.2. $A_T$ determination and reconstruction

Discrete seawater samples were analysed for  $A_T$  by using a VINDTA 3C and following the procedure detailed by Mintrop et al., (2000). The VINDTA 3C was calibrated through the titration of Certified Reference Material (CRMs; provided by A. Dickson at Scripps Institution of Oceanography), giving values with an accuracy of  $\pm 1.5 \mu\text{mol kg}^{-1}$ .

An empirical salinity-based relationship was developed to reconstruct  $A_T$  specifically for the monitored transect. The  $A_T$ -SSS linear relationship (Eq. 1), derived from 46 discrete samples, is statistically significant at the 99% level of confidence ( $p$ -value  $< 0.01$ ) and present a high degree of correlation ( $r^2 = 0.99$ ) and a root mean square error (RMSE) of  $\pm 5.6 \mu\text{mol kg}^{-1}$ .

$$A_T = 100.5 (\pm 2.9) \text{ SSS} - 1271 (\pm 108) + \varepsilon \quad (1)$$

Although the reconstruction of  $A_T$  from its linear relationship with SSS does not account for biological processes that cannot be traced with salinity (Wolf-Gladrow et al., 2007), nor the input of dissolved carbonate minerals and bicarbonate-carbonate species from river runoff, sediments, and water mixing, it has been widely used. It provides useful general approximation in regions with stable conditions and limited influence from these processes. The strong correlation of the  $A_T$ -SSS linear relationship, and its consistency with those proposed for various regions of the Mediterranean Sea (Schneider et al., 2007; Copin-Montégut and Bégovic, 2002; Jiang et al., 2014; Cossarini et al., 2015), indicate a dominant control of salinity-driven processes over  $A_T$  variability. In the western Mediterranean, these processes primarily include the conservative effects of evaporation-precipitation balance and the inflow of cooler, less saline Atlantic waters (Jiang et al., 2014). River runoff also causes local changes in SSS, but its role as a salinity-independent source of  $A_T$  variability is minimal compared to the eastern Mediterranean basin (Jiang et al., 2014; Cossarini et al., 2015). With respect to biogeochemical processes, they cause negligible changes in salinity and induce small direct changes in  $A_T$ .

To account for minor variations in  $A_T$  independent on salinity, a non-conservative term ( $\varepsilon$ ) was included in the linear model (Eq. 1), representing the residuals (the difference between measured  $A_T$  values and those predicted from SSS), capturing variability not explained by salinity alone.  $A_T$  was calculated at the times of the SSS observations (Curbelo-Hernández et al., 2021a; 2021b; 2023) using Eq. 1. A *Monte Carlo* simulation was employed to propagate the uncertainties from both the linear model parameters (slope and intercept) and the  $\varepsilon$  term: 10,000 simulations were conducted for each SSS observation by generating random realizations of the regression parameters from normal distributions centered at their best-fit values with standard deviations equal to their respective standard errors. Similarly, random realizations of  $\varepsilon$  were performed from a normal distribution characterized by the mean and standard deviation of  $\varepsilon$ . This yielded a

full probability distribution of estimated  $A_T$  values for each observed SSS, from which the ensemble mean, standard deviation, and 95% confidence intervals were computed. The propagated uncertainty in  $A_T$  estimates, considering the errors in  $A_T$  determination and SSS measurements (Section 2.3) and the linear model uncertainty, was approximately  $\pm 5.7 \mu\text{mol kg}^{-1}$ . This error in  $A_T$  estimation falls within the accepted uncertainty range of  $\pm 10 \mu\text{mol kg}^{-1}$  for  $A_T$  when used as an input variable alongside  $f\text{CO}_{2,\text{sw}}$  (when its uncertainty is up to  $\pm 2 \mu\text{atm}$ ) for the calculation of other MCS variables aligning with the criteria for the “weather goal” level of measurement quality (Steinhoff and Skjelvan, 2020). This new  $A_T$ -SSS relationship is applicable for estimating  $A_T$  in surface seawaters within the western Mediterranean Sea that are predominantly influenced by conservative processes, and where non-salinity factors such as biological activity and fluvial inputs are limited. This includes waters with salinities in the range of 36 to 38.5.

#### 2.4.1.3. pH and $C_T$ calculation

The pH and  $C_T$  were calculated at the times of the underway observations by using the  $\text{CO}_{2\text{SYS}}$  programme developed by Lewis and Wallace, (1998) and run with the MATLAB software (van Heuven et al., 2011; Orr et al., 2018; Sharp et al., 2023). The  $f\text{CO}_{2,\text{sw}}$  and  $A_T$  were used as input  $\text{CO}_2$  system variables. The set of constant used for computations includes the carbonic acid dissociation constants of Lueker et al., (2000), the  $\text{HSO}_4$  dissociation constant of Dickson, (1990), the HF dissociation constant of Perez and Fraga, (1987) and the value of  $[B]_T$  determined by Lee et al., (2010). The effect of temperature on pH was removed by computation at a constant temperature of  $19^\circ\text{C}$ , which is the mean temperature within the observational period (referred as  $\text{pH}_{19}$ ). Further data adjustments and statistical procedures are detailed in Appendix A.

#### 2.4.2. Thermal and non-thermal $f\text{CO}_{2,\text{sw}}$

The relative influence of the thermal and non-thermal processes on the variation of  $f\text{CO}_{2,\text{sw}}$  has been addressed. The non-thermal processes mainly include the biological and carbonate pumps, circulation patterns and air-sea gas exchange (De Carlo et al., 2013). The collectively known methodology presented by Takahashi et al., (2002) with the experimentally-determined temperature effects on  $p\text{CO}_2$  for isochemical seawater of  $0.0423 ^\circ\text{C}^{-1}$  (Takahashi et al., 1993) was used. This procedure has been previously applied to ES-SOOP-CanOA data and detailed by Curbelo-Hernández et al., (2021a; 2021b). An

alternative procedure recently introduced by Fassbender et al., (2022) and detailed by Rodgers et al., (2023), modified from the Takahashi et al., (2002, 1993) framework, was also applied in this investigation. This updated method addresses the slightly variations in the thermal sensitivity of  $f\text{CO}_{2,\text{sw}}$  due to background chemistry (Wanninkhof et al., 1999, 2022), which introduces slightly difference between the observed seasonal cycle of  $f\text{CO}_{2,\text{sw}}$  and the calculated through the sum of its thermal and non-thermal components. The Takahashi et al. (2002) and Fassbender et al. (2022) procedures are referred hereinafter as T'02 and F'22, respectively.

The new approach in F'22 for the thermal component of  $f\text{CO}_{2,\text{sw}}$  ( $f\text{CO}_{2, \text{T FASS}}$ ) was computed from the annual means (denoted with the subscripts AM) of SSS,  $A_{\text{T}}$  and  $C_{\text{T}}$  at in situ temperature (Eq. 2) by using the  $\text{CO}_{2\text{SYS}}$  programme (Lewis and Wallace, 1998) for MATLAB (van Heuven et al., 2011; Orr et al., 2018; Sharp et al., 2023). Then, the thermal-driven change in  $f\text{CO}_{2,\text{sw}}$  ( $f\text{CO}_{2, \text{T anom}}$ ) can be calculated as the difference between the thermal component of  $f\text{CO}_{2,\text{sw}}$  ( $f\text{CO}_{2, \text{T FASS}}$ ) and the annual mean of  $f\text{CO}_{2,\text{sw}}$  (Eq. 3).

$$f\text{CO}_{2, \text{T FASS}} = \text{CO}_{2,\text{SYS}}(C_{\text{T,AM}}, A_{\text{T,AM}}, \text{SSS}_{\text{AM}}, \text{SST}) \quad (2)$$

$$f\text{CO}_{2, \text{T anom}} = f\text{CO}_{2, \text{T FASS}} - f\text{CO}_{2,\text{AM}} \quad (3)$$

The new approach in F'22 for the non-thermal component ( $f\text{CO}_{2, \text{NT FASS}}$ ) is given by the difference between the  $f\text{CO}_{2,\text{sw}}$  at the times of observations and the  $f\text{CO}_{2, \text{T anom}}$  (Eq. 4). The difference among  $f\text{CO}_{2, \text{NT FASS}}$  and the annual mean of  $f\text{CO}_{2,\text{sw}}$  provides the change in  $f\text{CO}_{2,\text{sw}}$  explained by non-thermal processes ( $f\text{CO}_{2, \text{NT anom}}$ ) (Eq. 5).

$$f\text{CO}_{2, \text{NT FASS}} = f\text{CO}_{2,\text{sw}} - f\text{CO}_{2, \text{T anom}} \quad (4)$$

$$f\text{CO}_{2, \text{NT anom}} = f\text{CO}_{2, \text{NT FASS}} - f\text{CO}_{2, \text{AM}} \quad (5)$$

Considering the seasonal amplitudes of  $f\text{CO}_{2,\text{T}}$  and  $f\text{CO}_{2,\text{NT}}$  ( $\text{d}f\text{CO}_{2,\text{T}}$  and  $\text{d}f\text{CO}_{2,\text{NT}}$ ), the relative importance of thermal and non-thermal processes was expressed by the T/B ratio ( $\text{d}f\text{CO}_{2,\text{T}}/\text{d}f\text{CO}_{2,\text{NT}}$ ), with values greater than 1 indicating that the temperature effect govern the  $f\text{CO}_{2,\text{sw}}$  variations.

#### 2.4.3. Factors controlling the seasonal amplitude of $f\text{CO}_{2,\text{sw}}$

The changes in the surface  $f\text{CO}_{2,\text{sw}}$  result from the combined variation in the physical and biochemical seawater properties. The seasonal variability of the surface  $f\text{CO}_{2,\text{sw}}$  was addressed by attending the partial contribution of SST, SSS,  $C_T$  and  $A_T$  (e. g. Takahashi et al., 2014). The influence of each driver was quantified by assuming linearity and employing a first-order Taylor-series deconvolution (Sarmiento and Gruber, 2006) given in Eq. 6 and previously used for  $p\text{CO}_2$  (Doney et al., 2009; Lovenduski et al., 2007; Takahashi et al., 1993; Turi et al., 2014) and pH (Fröb et al., 2019; García-Ibáñez et al., 2016; Pérez et al., 2021; Takahashi et al., 1993; Curbelo-Hernández et al., 2024).

The seasonal changes of each driver (SST, SSS,  $C_T$  and  $A_T$ ) in Eq. 7  $\left(\frac{dX}{dt}\right)$  were assumed as their difference between the times of the year in which  $f\text{CO}_{2,\text{sw}}$  was at its minimum and maximum (seasonal amplitudes) per months elapsed. Seasonal amplitudes were calculated between monthly means (based on observations and computed data) for February and September (where minimum and maximum  $f\text{CO}_{2,\text{sw}}$  were observed). An error propagation based on standard deviations for February and September was performed to calculate the error of the seasonal change.

Due to the high relevance of the evaporation/precipitation processes in the Mediterranean Sea and in order to avoid the influence of freshwater fluxes, the most recent equation (Eq. 7) given by Pérez et al., (2021) with salinity-normalized  $C_T$  and  $A_T$  ( $\text{NC}_T$  and  $\text{NA}_T$ ) was used. The normalization was performed to a reference salinity ( $\text{SSS}_0$ ) of 37.4 ( $\text{NC}_T = \text{SSS}_0 * C_T / \text{SSS}$ ;  $\text{NA}_T = ((A_T - 728.3) / \text{SSS}) * \text{SSS}_0 + 728.3$ , following Friis et al., 2003), which is the average SSS for the entire monitored area.

$$\frac{df\text{CO}_2}{dt} = \frac{\partial f\text{CO}_2}{\partial \text{SST}} \frac{d\text{SST}}{dt} + \frac{\partial f\text{CO}_2}{\partial \text{SSS}} \frac{d\text{SSS}}{dt} + \frac{\partial f\text{CO}_2}{\partial C_T} \frac{dC_T}{dt} + \frac{\partial f\text{CO}_2}{\partial A_T} \frac{dA_T}{dt} \quad (6)$$

$$\frac{df\text{CO}_2}{dt} = \frac{\partial f\text{CO}_2}{\partial \text{SST}} \frac{d\text{SST}}{dt} + \left( \frac{\partial f\text{CO}_2}{\partial \text{SSS}} + \frac{\text{NC}_T}{\text{SSS}_0} \frac{\partial f\text{CO}_2}{\partial C_T} + \frac{\text{NA}_T}{\text{SSS}_0} \frac{\partial f\text{CO}_2}{\partial A_T} \right) \frac{d\text{SSS}}{dt} + \frac{\text{SSS}}{\text{SSS}_0} \frac{\partial f\text{CO}_2}{\partial C_T} \frac{d\text{NC}_T}{dt} + \frac{\text{SSS}}{\text{SSS}_0} \frac{\partial f\text{CO}_2}{\partial A_T} \frac{d\text{NA}_T}{dt} \quad (7)$$

It is important to remark that the changes in  $\text{NA}_T$  and  $\text{NC}_T$  are linked with biogeochemical processes which have different influences: the processes involved in the organic carbon pump contribute to strongly change the  $\text{NC}_T$  weakly affecting the  $\text{NA}_T$ , while those involved in the carbonate pump affect the  $\text{NA}_T$  twice as much as  $\text{NC}_T$ . The positive values

of  $\frac{dfCO_2}{dt}$  and  $\frac{\partial fCO_2}{\partial x} \frac{dx}{dt}$  indicate an increase in  $fCO_{2,sw}$  from February to September, while negative values the opposite.

#### 2.4.4. Air-sea CO<sub>2</sub> fluxes

The air-sea CO<sub>2</sub> fluxes (FCO<sub>2</sub>) were determined using the bulk formula in Eq. 8:

$$FCO_2 = 0.24 K_0 K_{660} \Delta fCO_2 \quad (8)$$

where  $K_0$  is the solubility of CO<sub>2</sub> in seawater,  $K_{660}$  is the gas transfer velocity and  $\Delta fCO_2$  represents the difference between  $fCO_{2,sw}$  and  $fCO_{2,atm}$ . A conversion factor of 0.24 was used to express FCO<sub>2</sub> values in units of mmol m<sup>-2</sup> d<sup>-1</sup>.  $K_0$  was calculated by using the equation and coefficients given by Weiss, (1974) and measured SST and SSS which fall within the valid application limits. Considering the fitting error from the original parameterization of  $K_0$  ( $\pm 1 \times 10^{-4}$  mol L<sup>-1</sup> atm<sup>-1</sup>; Weiss, 1974) and the instrumental errors of SST and SSS measurements (section 2.3), the uncertainty associated with the solubility estimation had a negligible impact on the calculation of FCO<sub>2</sub>.  $K_{660}$  was calculated through its quadratic dependency with wind speed (Eq. 9) using the parametrization given by Wanninkhof (2014):

$$K_{660} = 0.251 \cdot w^2 \cdot \left( \frac{Sc}{660} \right)^{-0.5} \quad (9)$$

where  $w$  is the wind speed and  $Sc$  is Schmidt number (cinematic viscosity of seawater, divided by the gas diffusion coefficient). ERA5 hourly wind speed reanalysis data at 10 m above the sea level and with a spatial resolution of 0.25° x 0.25° (Hersbach et al., 2023) were used to calculate  $K_{660}$ . The ERA5 reanalysis for the global climate and weather is available at Copernicus Climate Data Store (<https://cds.climate.copernicus.eu/>; last access: 15 May 2025). The uncertainty in  $K_{660}$  reported by Wanninkhof (2014) when using wind speeds ranging between 3 and 15 m s<sup>-1</sup> is  $\pm 20\%$ . The error in the determination of  $fCO_{2,sw}$  and  $fCO_{2,atm}$  (Section 2.4.1) propagates into the calculation of  $\Delta fCO_2$  and constitutes an additional source of uncertainty. The statistical procedure used to quantify the uncertainty in the FCO<sub>2</sub> arising from the uncertainty in  $\Delta fCO_2$  is described in Appendix B. The mean absolute error in FCO<sub>2</sub> due to the propagated uncertainty of  $\Delta fCO_2$  ( $\pm 2.01$   $\mu$ atm) was  $\pm 0.14$  mmol m<sup>-2</sup> d<sup>-1</sup>, which in relative term is  $\pm 0.05\%$ . Negative FCO<sub>2</sub>

values indicate that the ocean acts as an atmospheric CO<sub>2</sub> sink, while the positive ones indicate that it behaves as a source.

### 3. Results

A total amount of 157,984 data for surface ocean  $x\text{CO}_2$  were collected during the study period (34,015 data during 2019, 28,590 data during 2020, 33,288 data during 2021, 19,102 data during 2022, 39,738 data during 2023 and 3,251 data during January and February 2024). This amount exceeds the total number of data points available in the historical record for the Western Mediterranean (34.8–43.1°N, 5.5°W–4.7°E) since 1999 (146,094 data) available in SOCAT v2024 (Bakker et al., 2016, 2024). The total number of data points in this region included in the SOCAT v2024 database since 2019 is 44,520.

Due to differences in the spatial distribution of observations, two subregions (referred to as sections) were identified along the vessel track (Figure 1): the longitudinally distributed southern section (hereinafter S section), accomplishing the Alboran Sea (~2–5.1°W), and the latitudinally distributed east section (hereinafter E section), following the eastern coastline of the Iberian Peninsula (~36.5–41.3°N). The spatiotemporal distribution of  $f\text{CO}_{2,\text{sw}}$  and the total number of data points available in each dataset for sections S and E is shown in Figure Sup2. In the S section,  $f\text{CO}_{2,\text{sw}}$  values from ES-SOOP-CanOA station are consistent with those in SOCAT v2024, although the limited number of cruises covering this section in SOCAT v2024 difficult a direct comparison and prevent robust characterization of spatial and seasonal variability patterns. In the E section, some differences between the two datasets are observed (i. e. during spring–summer 2021,  $f\text{CO}_{2,\text{sw}}$  was higher in SOCAT v2024 than in the ES-SOOP-CanOA dataset). These differences are mainly explained by the distinct sampling trajectories in SOCAT v2024, with some routes extending further eastward, including coastal areas around the Balearic Islands.

The spatial distribution of the average values allowed to identify heterogeneity in the annual cycle of each variable along both sections (Figure 2 and Sup3). The standard deviation of the spatially-averaged variables is presented in Table Sup2. A strong west-to-east increasing gradient in SST was observed in summer through the S section (~5.5°C) which lead an increment in  $f\text{CO}_{2,\text{sw}}$  of ~57.5  $\mu\text{atm}$  and a depletion in pH of ~0.040 units eastward across the Alboran Sea. Despite the approximately constant SST through the S



section during the rest of the year (less than 1.5°C of difference between the western and easternmost parts), an eastward decrease in  $f\text{CO}_{2,\text{sw}}$  of less than 18  $\mu\text{atm}$  accompanied by an increase in pH of less than 0.030 units was observed between October and March.

The latitudinal gradient of SST through the E section was weaker throughout the year, keeping spatially stable the  $f\text{CO}_{2,\text{sw}}$  and pH. The maximum change in SST occurs during winter, in which a northward decrease of less than 2°C explained minimum seasonal average temperatures and  $f\text{CO}_{2,\text{sw}}$  through the cruise track (14-15 °C and 350-360  $\mu\text{atm}$ , respectively). It contrasts with the maximum average temperatures and  $f\text{CO}_{2,\text{sw}}$  encountered during summer (25.0-26.5 °C and 450-470  $\mu\text{atm}$ , respectively). These results reported that the maximum amplitude of the seasonal cycle of SST,  $f\text{CO}_{2,\text{sw}}$  and pH occurs along the eastern coastline of the Iberian Peninsula and specially over the continental shelf between Valencia and Barcelona (northernmost part of E section), while the minimum seasonal amplitude occurs near the Strait of Gibraltar (westernmost part of the S section).

The spatial variation in  $C_T$  were significant throughout the year along both sections (Figure 2). The  $C_T$  increases eastward in the order of 20-45  $\mu\text{mol kg}^{-1}$  along the S section throughout the year. This increment accelerated along the E section from Cape of Gata to Cape of Nao and become approximately stable from Cape of Nao to Barcelona port. The spatial distribution of  $C_T$  was highly influenced by the progressively salinification observed along the S section. The SSS increased during the entire annual cycle from 36.3-36.5 around the eastern part of the Strait of Gibraltar to 37.7-38.1 around Cape of Nao (Figure Sup3). Removing the effect of salinity, the  $\text{NC}_T$  (Figure Sup3) presents a weaker spatial variation through the vessel track mainly lead by biological and mixing processes.

The surface physico-chemical properties show heterogeneities during some seasons of the year among several key locations along the sections (Figure 2 and Sup3). The heterogeneities in the temporal evolution of the SST, SSS and  $\text{CO}_2$  system variables was assessed by the strategic selection of 5 stations along the S section (stations S1-S5) and 6 stations along the E section (stations E1-E6), geographically depicted in Figure 1. The S1 ( $4.95 \pm 0.05$  °W) occupied the easternmost part of the Strait of Gibraltar, the S2-S4 ( $4.35 \pm 0.05$  °W,  $3.85 \pm 0.05$  °W and  $2.95 \pm 0.05$  °W) were placed in the central Alboran Sea and the S5 ( $2.45 \pm 0.05$  °W) located south of Cape of Gata. The stations along the E section include E1 ( $37.1 \pm 0.2$  °N) in the Gulf of Mazarron, E2 ( $37.6 \pm 0.2$  °N) to the east

of Cape of Palos, E3 ( $38.2 \pm 0.2$  °N) in the Gulf of Alicante, E4 ( $38.7 \pm 0.2$  °N) to the east of Cape of Nao, E5 ( $39.3 \pm 0.2$  °N) in the Gulf of Valencia over the continental slope, and E6 ( $40.2 \pm 0.2$  °N) near the Ebro estuary over the continental shelf.

The temporal variations of each variable at S1-S5 and E1-E6 are depicted in Figure 3, 4, Sup4, Sup5 and Sup6. The seasonal amplitudes and interannual trends are summarized in Table 1. The seasonal amplitude of SST (minimum values in February-March around 14-17 °C and maximum values in August-September around 20-26°C) increased eastward through the S section although the local decrease at S2 (Figure 3 and Sup4, Table 1). The seasonal changes were larger through the E section (~14 to ~28°C) and show weaker spatial variations (Figure 4 and Sup5, Table 1). The SSS (Figure Sup6), do not exhibit a seasonal cycle well-correlated to the harmonic function in Eq. A.1 ( $r^2 < 0.5$ ; Table Sup2). The lower and more spatially stable SSS values were observed along the S section during the entire period (around 36.0-37.5), while increase with latitude through the E section (around 36.7-38.1).

The seasonal amplitude of  $f\text{CO}_{2,\text{sw}}$  (from ~340 to ~460  $\mu\text{atm}$  in the S section and from ~340 to ~470  $\mu\text{atm}$  in the E section) and pH (from ~8.00 to ~8.12 units in the S section and from ~8.00 to ~7.98 to ~8.13 units in the E section) was strongly linked with those of SST. It exhibits a west-to-east increment through the S section with the exception at S2 (Figure 3 and Sup4, Table 1) and remained approximately constant through the E section (Figure 4 and Sup5, Table 1). These spatial heterogeneities in the seasonal cycles were found to be leaded by the different rise in SST during late summer along each section as minimal spatial differences were observed during the rest of the year.

The  $C_T$  (Figure Sup6) seasonally decreased from January-February to September-October (from ~2180 to ~2085  $\mu\text{mol kg}^{-1}$  in the S section and from ~2260 to ~2105  $\mu\text{mol kg}^{-1}$  in the E section) in phase with the enhancement biological production. The seasonal amplitude of  $C_T$  increased eastward through the S section and northward through the E section, following the salinification gradient (Figure Sup6, Table 1). Once removed the effect of salinity, the seasonal cycle of  $\text{NC}_T$  shows minimal differences in the S section between the western and the easternmost part, while in the E section the  $\text{NC}_T$  and its seasonal amplitude increased northward (Figure Sup6, Table 1). The enhanced adjustment (correlation) of  $\text{NC}_T$  with Eq. A.1 ( $0.47 < r^2 < 0.61$  at S section and  $0.70 < r^2 < 0.88$  at E section) compared to  $C_T$  ( $0.28 < r^2 < 0.56$  at S section and  $0.45 < r^2 < 0.73$  at E section)

emphasizes the relevance of the processes varying salinity. The lower correlations encountered through the S section shows the higher impact of eventual processes (i. e. changes in the evaporation/precipitation, river runoff, mesoscale features) locally modifying the surface carbon system in this area and introducing spatial heterogeneities in their seasonal cycles.

## **4. Discussion**

### **4.1. Spatial characterization of the CO<sub>2</sub> system and its seasonality**

#### **4.1.1. The Alboran Sea**

The seasonal variability of the AJ (García-Lafuente et al., 2002; Macías et al., 2008, 2016; Vargas-Yáez et al., 2002) modified the SST signature in the S section, thus influencing  $f\text{CO}_{2,\text{sw}}$  and pH. The maximum intensity of the AJ during summer (Peliz et al., 2013; Renault et al., 2012) caused a more intense warming and salinification of MAW while advancing into the Mediterranean Sea and mixing with the fraction of MW which surround the Cape of Gata and recirculate westward (Millot, 1999; Sánchez-Garrido et al., 2013). It explained the eastward increase in  $f\text{CO}_{2,\text{sw}}$  and decrease in pH at this time of the year (Figure 2; Section 3.1).

The relatively low SST and  $f\text{CO}_{2,\text{sw}}$  around S1 ( $20.68 \pm 2.20$  °C and  $401.68 \pm 27.13$   $\mu\text{atm}$ ) and S3 ( $21.15 \pm 2.11$  °C and  $407.30 \pm 26.20$   $\mu\text{atm}$ ) were mainly due to the highest intensity of the wind-induced upwelling along the northern coast of the western Alboran Sea during the warm season. It cooled the surface and enhanced the biological drawdown (e. g. Bolado-Penagos et al., 2020; Folkard et al., 1997; Gómez-Jakobsen et al., 2019; Peliz et al., 2009; Richez and Kergomard, 1990; Stanichny et al., 2005), while favouring the formation of the cold and nutrient-rich filament separating the WAG and EAG (Gómez-Jakobsen et al., 2019; Millot, 1999). Differences in the influence and strength of this filament may contributed to the observed heterogeneities in SST,  $f\text{CO}_{2,\text{sw}}$ , and pH at S1 during the warm seasons (Figure 3), which in turn account for reducing the model fitting performance. Additionally, the shallowest position of the AMI during late-winter (De La Paz et al., 2009; Echevarría et al., 2002; Gómez-Jakobsen et al., 2019; Minas et al., 1991) feed the surface with CO<sub>2</sub>-rich waters coming from deeper areas in the Mediterranean Sea (De La Paz et al., 2009; Echevarría et al., 2002; Gómez-Jakobsen et al., 2019; Minas et al., 1991), elevating  $f\text{CO}_{2,\text{sw}}$  around S1. The increase in  $C_T$  and  $\text{NC}_T$  during summer around S3 (Figure 2 and Sup3), which contributed to reduce their seasonal

amplitudes in this area (Figure Sup6, Table 1), suggests that the upwelled waters transported by the filament at this time of the year were not enough remineralized to compensate the SST-driven decrease in  $f\text{CO}_{2,\text{sw}}$ . In consequence, the western and eastern edges of the WAG presented the shortest seasonal amplitudes along the S section for SST,  $f\text{CO}_{2,\text{sw}}$  and pH (Figure 3; Table 1).

Conversely, the increase in SST and  $f\text{CO}_{2,\text{sw}}$  during summer around S2 ( $22.63 \pm 2.05$  °C and  $429.98 \pm 24.86$   $\mu\text{atm}$ ), S4 ( $23.89 \pm 2.03$  °C and  $438.25 \pm 25.22$   $\mu\text{atm}$ ) and S5 ( $24.05 \pm 1.61$  °C and  $441.67 \pm 16.22$   $\mu\text{atm}$ ) contributed to extend their seasonal amplitudes in these zones (Figure 2 and 3; Table 1). It suggest that, during the warm season, the increase in  $f\text{CO}_{2,\text{sw}}$  leaded by the surface warming near the core of the gyres was not compensated by the biological drawdown occurring at this time of the years (which caused a weak decrement in  $C_T$  and  $\text{NC}_T$  at S2; Figure 2 and Sup3).

#### **4.1.2. The Eastern Iberian margin**

The eastern coastal transitional area of the Iberian Peninsula was subject to variability related with changes in the intensity, morphology and path of the Northern Current (Figure 1b). The SST decreased in the northernmost part of the E section from Sagunto to Barcelona throughout the year (north of S5; Figure 2). The cooling of this area intensified during the cold season due to the mixing of warm waters in the wind-shielded area North of Cape of Nao with cool and salty MW transported by the Northern Current. However, it weakened during the warm season due to the northward spreading of MAW favoured by the formation of the thermal front in the axis of the Pyrenees, changing the path of the Northern Current (López-García et al., 1994). In the southernmost part of the section, the enhanced northward spreading of MAW and less wind stress during summer drives the warming observed from Cape of Gata (at S5) to Cape of Nao (at E4), while a low intense branch of the Northern Current transporting MW and progressing southward Cape of Nao weakly cool the area during winter (López-García et al., 1994; López-Jurado et al., 1995).

The local decrease in SST and  $f\text{CO}_{2,\text{sw}}$  observed during the warm seasons at E4 traced the offshore recirculation of the Northern Current at Cape of Nao (Millot, 1999) and separating the E section within its northern and southernmost areas. This division was also evidenced based on the  $C_T$  and  $\text{NC}_T$  signatures (Figure 2 and Sup6): the northernmost

part of the section receives remineralized MW transported by the Northern Current which elevates  $C_T$  and  $NC_T$ , while the southernmost part was supplied with recent MAW with relatively low  $C_T$  and  $NC_T$ . Additionally, Ulses et al. (2023) recently suggested that the convective area in the Gulf of Lion behaves as a source of natural and anthropogenic carbon to the intermediate waters of the western Mediterranean, which can enter the surface through vertical mixing and account for the observed high amount of  $C_T$  and  $NC_T$ .

Although the spatial heterogeneities and the northward cooling during the cold season (Figure 1) increasing seasonal changes in SST, the seasonal amplitudes of  $fCO_{2,sw}$  keep approximately constant within E1-E6 (Figure 3 and Sup5; Table 1). The location of station E5, away from the influence of the Northern Current during the warm months, explained its locally lower seasonal amplitudes compared to adjacent waters in the northernmost part of E section. Nevertheless, these heterogeneities were minimal and do not caused differences in the seasonal amplitude of pH (Table 1).

In the case of  $C_T$  and  $NC_T$  (Figure Sup6, Table 1), the enhancement in the mixing of MAW with MW during winter increased northward the seasonality from E1 to E4. In the northernmost part, the seasonal variations in  $C_T$  and  $NC_T$  become shorter due to their increment during the cold season. It was caused by the combined action of the enhanced arrival of remineralized MW at this time of the year and the mesoscale structures locally favouring injections of  $CO_2$ -rich deeper waters into the surface (Bosse et al., 2021; Millot, 1999). The Ebro River runoff peaking among late-winter and spring (Zambrano-Bigiarini et al., 2010) can also behaves as a source of variability around E5-E6.

#### **4.2.Warming and interannual trends of MCS variables**

The monitoring of the surface Western Mediterranean Basin allowed the identification of interannual trends for physical and MCS properties (Table 1 and 2). The SST increased at a rate of  $0.38 \pm 0.05 \text{ } ^\circ\text{C yr}^{-1}$  in the S section and  $0.30 \pm 0.04 \text{ } ^\circ\text{C yr}^{-1}$  in the E section. The rate of increase in SST locally intensified at S2 ( $0.50 \pm 0.09 \text{ } ^\circ\text{C yr}^{-1}$ ) may be due to the transport and accumulation of surface waters toward the core of the WAG. Its variability, migration and progressively collapse can also account for the rapid warming of the area (Sánchez-Garrido et al., 2013; Viúdez et al., 1998; Vélez-Belchí et al., 2005).

The SST trends based on ES-SOOP-CanOA data were of the same order of magnitude as those derived from reanalysis data for the period 2019–2024, but were one order of magnitude higher than the reanalysis-based trends for 2000–2019, indicating a reinforcement of sea surface warming by approximately 80–90% (Table 1). The ES-SOOP-CanOA data-based interannual SST trends were found to be reinforced during summer by 55.2% in the S section and by 32.4% in the E section compared to winter. The Northern Current cooling the northernmost part of the E section accounted to decelerate the warming in comparison to the S section. The ES-SOOP-CanOA data-based trends reported a cumulative increase in SST from 2019 to 2024 of  $1.91 \pm 0.26$  °C in the Alboran Sea (S section) and  $1.52 \pm 0.22$  °C along the eastern Iberian margin (E section). These cumulative increments were 48.3% and 34.94% respectively higher than those estimated for the global surface ocean from 1850-1900 to 2001-2020 ( $0.99 \pm 0.12$  °C; IPCC, 2023). It aligns with projections from climate models for both terrestrial and marine environments in the mid latitudes, particularly within the Mediterranean region, in consequence of human-induced global warming, which was detailed by Hoegh-Guldberg et al., (2018) in the AR6 Synthesis Report (IPCC, 2023).

The warming contributes to modify the MCS dynamics, mainly accelerating the increase in  $f\text{CO}_{2,\text{sw}}$  and acidification. The interannual trends of  $f\text{CO}_{2,\text{sw}}$  and pH (Table 1) were more than twice (except for trends at S1) than those reported for the Northwestern Mediterranean at the DYFAMED site based on the difference between average observation-based data for the periods 1995-1997 and 2013-2015 ( $2.30 \pm 0.23$   $\mu\text{atm yr}^{-1}$  and  $-0.0022 \pm 0.0002$  units  $\text{yr}^{-1}$ ; Merlivat et al., 2018) and for the Northeast Atlantic at the ESTOC site based on in situ measurements since 1995 ( $2.1 \pm 0.1$   $\mu\text{atm yr}^{-1}$  and  $0.002 \pm 0.0001$  units  $\text{yr}^{-1}$ , respectively; González-Dávila and Santana-Casiano, 2023). The interannual rates accelerated eastward along the S section and northward along the E section (Table 1). The stronger trends at S3 compared to adjacent waters (S2 and S4) may be due to the transport of  $\text{CO}_2$ -rich waters from the southern Iberian coast through the filament. The trends in the S section were conducted by the larger rates of change encountered during the warm season compared to the cold season. The opposite occurred in the E section, where an intense increase in  $f\text{CO}_{2,\text{sw}}$  accompanied by a drawdown in pH occurred during winter and trends were reversed during summer (Table 1).

These spatial differences among the cold and warm seasons were mainly linked with variations in the biological production/remineralization and mixing and were independent of the surface ocean warming. Hence, they were required to be assessed together with the  $NC_T$  trends for a better understanding. The  $NC_T$  interannually decreases throughout the region (Table 2). The rapid depletion in the S section during winter in comparison to summer could be due to, first, an interannual weakening in remineralization processes and/or inputs of  $CO_2$ -rich water to the area during the cold months, and second, an interannual strengthened in the biological uptake during the warm months. However, these variations resulted insufficient to compensate the increase in  $fCO_{2,sw}$  and subsequent fall down in pH induced by warming during the cold and even more during the warm months. Conversely, in the E section, the variations in lateral/vertical advection, primary driven variations in the (sub)mesoscale structures (Alberola et al., 1995; Bosse et al., 2021; 2016; Bourg and Molcard, 2021), were of high-relevance and introduced differences in the annual cycle of  $NC_T$ . The interannual variations during winter were minimal (Table 1, Figure Sup6), likely due to not significant changes in remineralization and in the dissolved  $CO_2$  concentration of waters transported into the area. The decrease in  $NC_T$  intensified during summer (Table 1, Figure Sup6) likely caused by the enhancement in biological production together with the dismissing lateral advection (this may be related with a reinforcement in the front formed in the axis of the Pyrenees due to the increasingly higher SST of the MAW).

Once removed the effects of temperature, the interannual  $pH_{19}$  trends overturned to negligible and were not statistically significant in the S section ( $< -0.001$  units  $yr^{-1}$ ; p-values  $> 0.1$ ). It suggests that warming is directly driving the acidification (and indirectly by rising  $fCO_{2,sw}$ ) while the progressively enhancing in biological productivity partially compensates for the expected fall down in pH. In the E section,  $pH_{19}$  were reduced by 63% ( $-0.002 \pm 0.001$  units  $yr^{-1}$ ; p-values  $< 0.01$ ) in comparison to the pH trends, which explains that the increase in SST is contributing more than half on the acidification due to only the atmospheric  $fCO_2$  increase. The negative  $pH_{19}$  trends reinforced in the E section by 47% during the cold season due to the enhancement in remineralization. The  $pH_{19}$  trends reversed to positive during the warm season due to the important role of biological production actively reducing  $fCO_{2,sw}$  and rising pH at this time of the year.

However, despite the high statistical confidence in the trends and the consistency found with reanalysis products, the acceleration in surface warming and consequent changes in  $f\text{CO}_{2,\text{sw}}$  and pH observed may be linked to isolated extreme events such as marine heat waves and are not necessarily indicative of prolonged behaviours over time. The globally increased frequency and magnitude in marine heat waves in phase with warming (Oliver et al., 2018; Hoegh-Guldberg et al., 2018; Frölicher et al., 2018; Smale et al., 2019) could feedback and hence continue expediting the surface ocean warming. The influence of these extreme events is especially relevant in semi-enclosed seas as the Mediterranean, recognized as one of the most affected marine areas in the yearly Copernicus Ocean State Reports (OSR; EU Copernicus Marine Service; <https://marine.copernicus.eu/access-data/ocean-state-report>; last access: 15 May 2025) since 2016 (OSR1-OSR7).

#### **4.3. The relative contribution of thermal and non-thermal processes on the surface $f\text{CO}_{2,\text{sw}}$**

The temporal evolution of  $f\text{CO}_{2,\text{sw}}$  due to thermal and non-thermal effect ( $f\text{CO}_{2,\text{T}}$  and  $f\text{CO}_{2,\text{NT}}$ , respectively) showed a high degree of agreement between the T'02 and F'22 methodologies (Figures 3 and 4). The average  $f\text{CO}_{2,\text{T}}$  and  $f\text{CO}_{2,\text{NT}}$  values differed by less than 5  $\mu\text{atm}$  between the two methodologies. The consistency with the widely employed T'02 engenders confidence in the validity and reliability of the most updated F'22 method.

The seasonal variations in  $f\text{CO}_{2,\text{sw}}$  were close to twice in the E section compared to the S section (Table 1). The thermal-driven seasonal changes ( $d f\text{CO}_{2,\text{T}}$ ) were found to approximately double those independent of temperature ( $d f\text{CO}_{2,\text{NT}}$ ) throughout the region (Table 2). The T/B ratios demonstrated the control of thermal processes over the seasonality of  $f\text{CO}_{2,\text{sw}}$  throughout the region (Table 2). The T/B ratios in the westernmost part of the S section (ranged between 1 and 2) were consistent with previous studies in the Strait of Gibraltar (Curbelo-Hernández et al., 2021b; De La Paz et al., 2009). The T/B ratios increased eastward as the AJ advanced in the Alboran Sea and caused by the intense increase in  $d f\text{CO}_{2,\text{T}}$  compared to  $d f\text{CO}_{2,\text{NT}}$ . They exceeded 2 in S4-S5 and E1-E6, which demonstrated the larger control of SST over  $f\text{CO}_{2,\text{sw}}$  in areas less influenced by the input of surface Atlantic water.



The interannual trends show the control of thermal processes over the increase in  $f\text{CO}_{2,\text{sw}}$  during 2019-2024 (Figure 3 and 4; Table 2). The strong and statistically significant interannual  $f\text{CO}_{2,\text{T}}$  trends show the important role of warming in elevating  $f\text{CO}_{2,\text{sw}}$ . The weak and non-significant  $f\text{CO}_{2,\text{NT}}$  trends suggest that spatio-temporal variations in the biological processes, circulations patterns and air-sea gas exchange introduced local differences in the distribution of  $f\text{CO}_{2,\text{sw}}$ . It difficult to assess the impact of the non-thermal processes on an interannual scale at each of the stations. The interannual trends of  $f\text{CO}_{2,\text{T}}$  and  $f\text{CO}_{2,\text{NT}}$  for the entire S and E sections (Table 2) were statistically significant at more than the 95% level of confidence and its coupling described, with less than  $0.3 \mu\text{atm yr}^{-1}$  of difference ( $<1\%$ ), the interannual rates of  $f\text{CO}_{2,\text{sw}}$  during 2019-2024 (Table 1; section 4.2).

The thermal processes govern the changes in  $f\text{CO}_{2,\text{sw}}$  on an interannual scale with a contribution ranged between  $\sim 76\text{-}92\%$  in the S section and  $\sim 73\text{-}83\%$  in the E section. The contributions for  $f\text{CO}_{2,\text{NT}}$  were between  $\sim 8\text{-}25\%$  and  $\sim 17\text{-}27\%$ , respectively. The decrease in  $f\text{CO}_{2,\text{NT}}$  compensated by  $\sim 6\text{-}30\%$  the increase in  $f\text{CO}_{2,\text{sw}}$  at S1-S5 and E1-E2, while its increase contributed by  $\sim 24\text{-}53\%$  to rise  $f\text{CO}_{2,\text{sw}}$  at E3-E6. The negative  $f\text{CO}_{2,\text{NT}}$  trends in the S section were related to progressive enhancement in the biological uptake (mainly during spring/summer) not compensated by remineralization and/or vertical/lateral advections of remineralized waters (mainly during autumn/winter) in areas influenced by recent MAW. Conversely, the interannual increase in  $f\text{CO}_{2,\text{NT}}$  in the E section suggest that the supply of cool and remineralized MW along the path of the high-intense Northern Current surpasses the biological drawdown of surface  $\text{CO}_2$  and is accounting to accelerate the increase in  $f\text{CO}_{2,\text{sw}}$  on an interannual scale.

#### 4.4. Mechanism controlling the seasonal cycle of $f\text{CO}_{2,\text{sw}}$

To infer the causes of variations in the seasonal cycle of  $f\text{CO}_{2,\text{sw}}$  among the study period, the seasonal rates of change in  $f\text{CO}_{2,\text{sw}}$  ( $\frac{df\text{CO}_{2,\text{sw}}}{dt}$ , hereinafter  $d f\text{CO}_2$ ) were decomposed into their individual components ( $\frac{\partial f\text{CO}_{2,\text{sw}}}{\partial X} \frac{\partial X}{\partial t}$ , hereinafter  $d f\text{CO}_2^X$ ) as described in section 2.4.3 (Eq. 6 and 7). The results of solved Eq. 7 for each year at S1-S5 and E1-E6 are depicted in Figure 5. The uncertainty associated with the difference between the monthly means for each term and year was obtained through error propagation considering their individual standard errors and presented in Table Sup 3. The  $d f\text{CO}_2$  resulted from the

cumulative sum of the individual terms in Eq. 7 (indicated with subscript “sum”) matched the  $\text{d}f\text{CO}_2$  directly calculated from observations between both seasons (indicated with the subscript “obs”), which renders confidence to the methodology (Figure 5).

The SST was identified as the main driver of  $\text{d}f\text{CO}_2$  throughout the stations, accounting on average for 51-71% of its values over the study period. In some stations and specific years, this contribution occasionally dropped to ~45% or increased up to ~83%. In the S section (Figure 5a),  $\text{d}f\text{CO}_2^{\text{SST}}$  increased westward as MAW get warmed in the Alboran Sea, while the incursion of the filament locally cooled the surface and decreased  $\text{d}f\text{CO}_2^{\text{SST}}$  at S3. In the E section (Figure 5b),  $\text{d}f\text{CO}_2^{\text{SST}}$  increased northward and reach its maximum north of Cape of Nao (at E4-E6), particularly during 2021-2022 ( $32.0\text{-}32.5 \mu\text{atm month}^{-1}$ ), due the higher influence of warmed MW.

The  $A_T$  described on average < 18% of  $\text{d}f\text{CO}_2$  in the entire region, occasionally increased up to 22%. As the  $f\text{CO}_{2,\text{sw}}$  inversely changes with  $A_T$ , the weakly negative  $\text{d}f\text{CO}_2^{\text{AT}}$  found for some years along the S section show fluctuations in the periods of increment and decrement of  $A_T$  likely related with changes in the mixing processes. The  $A_T$  contribution becomes negligible at E6 (<2% throughout the study period) due to the minimal seasonal amplitude of  $A_T$  and  $NA_T$  (Figure Sup6). The approximately constant  $A_T$  and  $NA_T$  levels throughout the year may be due to the bicarbonate and carbonate content from the Ebro River runoff being neutralized by those in MW and MAW, which spread into the area during winter and summer, respectively.  $\text{d}f\text{CO}_2^{\text{AT}}$  tend to decrease since 2020-2021 in S1-S3, S5 and E1 due to the progressively weakening in the  $NA_T$  depletion from February to September. The opposite occurred north of Cape of Palos, where the seasonal cycle of  $NA_T$  reaches its maximum amplitude ( $20\text{-}28 \mu\text{mol kg}^{-1}$  at E3 and E4). The interannual dealkalinization in S and E sections (Table 1) behaves as a source of heterogeneities: the interannual negative  $NA_T$  trends during the cold months ( $p\text{-values} < 0.01$ ) were stronger than during the warm months ( $p\text{-values} > 0.1$ ) and consistent in both sections. The spatial differences in the summer trends (weaker in the S compared to E section) account for an enhanced reduction of the seasonal amplitude of  $NA_T$  in the S section.

The  $\text{d}f\text{CO}_2^{\text{SSS}}$  were minimal in both the S and E sections (<0.6 and < 1.9  $\mu\text{atm month}^{-1}$ , respectively) and show the weak impact of SSS over  $\text{d}f\text{CO}_2$  (<3.5%). The entrance of MAW and its mixing with saltier MW in the Alboran Sea do not allow to identify a seasonal pattern in SSS (Figure Sup6), thus explained the negligible contribution of SSS

in the S section ( $\sim 2.0\%$  at S1 which fall down to  $<0.7\%$  at S2-S5). The larger seasonal amplitudes of SSS at E2-E5 (Figure Sup6) led a relatively major influence of SSS ( $\sim 1.0$ - $2.3\%$  during most of the years). The low seasonal amplitude of SSS and  $A_T$  at E6, likely related with an approximately constant influence of the Northern Current at this location throughout the annual cycle, caused a negligible variation in  $dfCO_2$  ( $<0.4\%$ ).

The depletion in  $C_T$ , mainly drove by the increased biological production from February to September, had a significant inverse impact on  $dfCO_2$  (23-37%). In 2019, at stations S1–S3 (and in 2020 only at S1), the inverse contribution of  $C_T$  reached for 39–47%. This suggests that the influence of the  $C_T$  cycle on  $dfCO_2$  in the westernmost Alboran Sea is increasingly resembling that observed in the rest of the Mediterranean. These findings indicate that the seasonal drawdown of  $C_T$  offsets between one-quarter and one-half of the expected increase in  $dfCO_2$  driven by SST and slightly prompt by  $A_T$ . In the S section (Figure 5a), the lower increase observed from 2019 to 2023 in  $dfCO_2^{CT}$  ( $4$ - $6\ \mu atm\ month^{-1}$ ) compared to  $dfCO_2^{SST}$  ( $6$ - $9\ \mu atm\ month^{-1}$ ) demonstrated that fluctuations in  $C_T$  were increasingly insufficient to counterbalance the warming-driven increase in  $dfCO_2$ , even at S2-S4 where the biological production enhanced and hence the  $dfCO_2^{CT}$  reinforced since 2020. In the westernmost part of the S section, the influence of  $C_T$  offsetting  $dfCO_2$  was maximum during 2019-2020 at S1 ( $>84\%$ ), S2 (67.3%) and S3 (86.1%) and diminished toward 2023 (37.1%, 38.3% and 45.1%, respectively). In the easternmost part, this compensation was around 33-44% at S4-S5 throughout the period (as at S2 and S3 since 2020) except for 2023 at S5, in which  $dfCO_2^{CT}$  weakened and offset only the 22.8%. In the E section (Figure 5b), the progressively strength in the processes depleting  $C_T$  throughout the period at E1-E4 and since 2020 at E5-E6 compensated by 33-46% the  $dfCO_2^{SST}$ , which changes inversely to  $dfCO_2^{CT}$ . The lowest compensation found in 2019 at E5 (28.8%) and E6 (18.4%) was likely related with eventual injections of remineralized waters along the Northern Current path, which offset the biological uptake of  $C_T$  and elevated the  $dfCO_2^{CT}$ .

#### 4.5. Air-sea $CO_2$ exchange across the Western Boundary of the Mediterranean Sea

The continuous observation of MCS variables enabled the calculation of  $FCO_2$  at an unprecedented high spatiotemporal resolution in the Western Mediterranean Sea. The  $FCO_2$  was found to be governed by fluctuations in  $\Delta fCO_2$  (Figure 6), mainly controlled

by the broader variability of  $f\text{CO}_{2,\text{sw}}$  (325-500  $\mu\text{atm}$ ) compared to  $f\text{CO}_{2,\text{atm}}$  (390-425  $\mu\text{atm}$ ). The SST fluctuations has a relevant role by primary controlling  $f\text{CO}_{2,\text{sw}}$  (section 4.3) and modulating the solubility of  $\text{CO}_2$  at the air-sea interface. The entire monitored area was undersaturated for  $\text{CO}_2$  respect to the low atmosphere between late October and June ( $\Delta f\text{CO}_2 = -35.30 \pm 8.97 \mu\text{atm}$ ), acting as an atmospheric  $\text{CO}_2$  sink ( $-2.56 \pm 0.55 \text{ mmol m}^{-2} \text{ d}^{-1}$ ) which peaks in winter ( $-4.53 \pm 0.44$  and  $-3.29 \pm 0.31 \text{ mmol m}^{-2} \text{ d}^{-1}$  in S and E sections, respectively). During summer, the area was supersaturated for  $\text{CO}_2$  ( $\Delta f\text{CO}_2 = 36.43 \pm 0.35 \mu\text{atm}$ ) and acted as a source, which was about three times more intense along the E section ( $1.70 \pm 0.43 \text{ mmol m}^{-2} \text{ d}^{-1}$ ) compared to the S section ( $0.57 \pm 0.35 \text{ mmol m}^{-2} \text{ d}^{-1}$ ).

The spatial differences in SST during warm months introduced heterogeneities in the seasonal outgassing among both sections: the higher SST during summer in the E section reduced the solubility and contributed to a higher increase in  $f\text{CO}_{2,\text{sw}}$  respect to  $f\text{CO}_{2,\text{atm}}$  ( $\Delta f\text{CO}_2 = 49.83 \pm 0.32 \mu\text{atm}$ ) compared to the cooler S section ( $\Delta f\text{CO}_2 = 16.35 \pm 0.14 \mu\text{atm}$ ). The seasonality in the formation of the  $\text{CO}_2$  sink and source in the Alboran Sea was consistent with previous studies in the Strait of Gibraltar (Curbelo-Hernández et al., 2021b; de la Paz et al., 2011, 2009) and Northwest African coastal transitional area in the Northeast Atlantic (Curbelo-Hernández et al., 2021a; Padin et al., 2010) and agreed with the seasonal pattern characteristic for tropical and subtropical regions (Bates et al., 2014; Takahashi et al., 2002). The warming during summer at S1 was insufficient to led supersaturated conditions ( $\Delta f\text{CO}_2 = -5.56 \pm 0.26 \mu\text{atm}$ ) and thus acted as a  $\text{CO}_2$  sink throughout the year ( $-2.83 \pm 1.77 \text{ mmol m}^{-2} \text{ d}^{-1}$  during cold months and  $-0.52 \pm 0.02 \text{ mmol m}^{-2} \text{ d}^{-1}$  during the warm months), which coincided with the behaviour observed in the Strait of Gibraltar during 2019 (Curbelo-Hernández et al., 2021b). The sink and source status during cold and warm months encountered in the Eastern Iberian Margin agreed with  $\text{FCO}_2$  evaluations based on observations in the Mediterranean basin through its northwestern (Wimart-Rousseau et al., 2023, 2021, 2020) and eastern parts (Sisma-Ventura et al., 2017), and confirms previous estimations based on satellite data and models (D'Ortenzio et al., 2008; Taillandier et al., 2012).

The variations in  $\text{FCO}_2$  during the period of study were addressed by averaging the data across seasons and years at each of the selected stations (Figure 7). The same procedure was applied to  $\Delta f\text{CO}_2$  and wind speed (Figure Sup7 and Sup8). The evolution of the

seasonal ingassing and outgassing was evaluated by computing interannual trends for average  $\text{FCO}_2$  and  $\Delta f\text{CO}_2$  (Figure 7). The interannual  $\text{FCO}_2$  trends evidenced the progressively strength of the summer source in the S section, which was accelerated at S2 in response to the enhanced warming around the WAG (detailed in section 4.2) and at S4-E1 due to their exposition to increasing wind forcing (Figure Sup7 and Sup8). It was caused by the increase in  $f\text{CO}_{2,\text{sw}}$  during the warm months not offset by biological drawdown which elevated  $\Delta f\text{CO}_2$ . In contrary, the localization of E2-E6 over the eastern Iberian continental shelf and slope allowed the relevant biological uptake at this time of the year to compensate for the influx of  $\text{CO}_2$ -rich water. It introduced heterogeneities in  $\Delta f\text{CO}_2$  between years which do not allow to identify statistically significant trends.

During spring and autumn, the increase in  $\Delta f\text{CO}_2$ , mainly driven by warming, accompanied by the decreasing wind stress (Figure Sup7 and Sup8), led the positive interannual  $\text{FCO}_2$  trends at S2-S5 and E1-E6 (Figure 7). They show the weakening in the ingassing during autumn and the achievement of a near-equilibrium state with the atmosphere during spring by the end of the study period. The  $\text{FCO}_2$  reversed to weakly positive during spring 2023 in the E section, which prolonged the seasonal source period having a relevant impact on the net annual  $\text{FCO}_2$ . During winter, the increasing wind forcing compensated the reduction in the ingassing expected by the rise in  $\Delta f\text{CO}_2$  (Figure Sup7 and Sup8). However, the variability in the wind speed and other processes involved in the non-thermal change of  $f\text{CO}_{2,\text{sw}}$  between years does not allowed the identification of statistically significant rates of change in the  $\text{CO}_2$  sink status. Particularly, the relatively high wind speed during winter 2021 may have contributed to accelerated horizontal transports, increasing  $f\text{CO}_{2,\text{sw}}$  and hence  $\Delta f\text{CO}_2$  (Figure Sup7 and Sup8).

The predominantly negative  $\text{FCO}_2$  during most of the year led a net annual  $\text{CO}_2$  sink behaviour. The positive  $\text{FCO}_2$  trends during summer, spring and autumn have forced the annual average  $\text{CO}_2$  invasion to decrease by 44-65% at S2-S5 (ranging from  $-0.66 \pm 0.06$  and  $-0.84 \pm 0.04 \text{ mol m}^{-2}$  during 2019 to  $-0.27 \pm 0.09$  and  $-0.47 \pm 0.09 \text{ mol m}^{-2}$  during 2023) and by 60-80% at E1-E6 (ranging from  $-0.32 \pm 0.09$  and  $-0.53 \pm 0.09 \text{ mol m}^{-2}$  during 2019 to  $-0.11 \pm 0.10$  and  $-0.13 \pm 0.09 \text{ mol m}^{-2}$  during 2023). The unique hydrodynamic of the Strait of Gibraltar strongly influenced the air-sea  $\text{CO}_2$  exchange at S1: the ingassing during summer partially compensated for the reduction of the annual

influx and resulted in a lower increase in  $\text{FCO}_2$  (23%) from 2019 ( $-0.77 \pm 0.02 \text{ mol m}^{-2} \text{ yr}^{-1}$ ) to 2023 ( $-0.60 \pm 0.06 \text{ mol m}^{-2} \text{ yr}^{-1}$ ).

Considering the annual average  $\text{FCO}_2$  for the S and E section, the net ingassing have decreased at a rate of  $0.11 \pm 0.02 \text{ mol m}^{-2} \text{ yr}^{-1} \text{ yr}^{-1}$  (p-value<0.01) in the Alboran Sea and by  $0.08 \pm 0.02 \text{ mol m}^{-2} \text{ yr}^{-1} \text{ yr}^{-1}$  (p-value<0.01) in the Eastern Iberian Margin. It contrast with the strength of the  $\text{CO}_2$  sink across the western Mediterranean basin recently reported by Zarghamipour et al., (2024) for 1984-2019 based on a combination of observational data and model simulations ( $0.007 \pm 0.001 \text{ mol m}^{-2} \text{ yr}^{-1} \text{ yr}^{-1}$ ). Additionally, Zarghamipour et al., (2024) noted the reduction of the annual net  $\text{CO}_2$  source behaviour of the Central Mediterranean basin at an estimated rate of  $0.003 \pm 0.001 \text{ mol m}^{-2} \text{ yr}^{-1}$ . The findings suggest that the acceleration in the increase in  $f\text{CO}_{2,\text{sw}}$  induced by the rapid warming, together with the progressive reduction in solubility, is reversing the interannual  $\text{FCO}_2$  trends compared to previous decades, may be causing the study area to be resemble the Central and Eastern Mediterranean basin in terms of air-sea  $\text{CO}_2$  exchange. The reduction of the net annual invasion was consistent with previous estimations in such coastal and shelf environments across the eastern tropical and subtropical South Atlantic during 2002-2018 (between  $0.03 \pm 0.01$  and  $0.09 \pm 0.02 \text{ mol m}^{-2} \text{ yr}^{-1} \text{ yr}^{-1}$ ; Ford et al., 2022) and toward mid-latitudes over the Scotian Shelf (with average  $\text{FCO}_2$  ranging from  $-1.7 \text{ mol m}^{-2} \text{ yr}^{-1} \text{ yr}^{-1}$  in 2002 to  $-0.02 \text{ mol m}^{-2} \text{ yr}^{-1} \text{ yr}^{-1}$  in 2006; Sisma-Ventura et al., 2017). The continuation of this decreasing rate for net annual ingassing would imply the reversion of the study area to a net annual  $\text{CO}_2$  source behaviour before 2030.

The net  $\text{CO}_2$  invasion was calculated by integrating the annual cycle of  $\text{FCO}_2$  during 2019-2023. The net  $\text{FCO}_2$  in the Alboran Sea was  $-1.57 \pm 0.49 \text{ mol m}^{-2} \text{ yr}^{-1}$ , which represented a strength in the  $\text{CO}_2$  sink in comparison with adjacent surface areas across the Strait of Gibraltar (between  $-0.82$  and  $-1.01 \text{ mol m}^{-2} \text{ yr}^{-1}$  during 2019-2021; Curbelo-Hernández et al., 2021) and the Eastern Iberian Upwelling ( $-1.33 \text{ mol m}^{-2} \text{ yr}^{-1}$ ; Chen et al., 2013). The net  $\text{FCO}_2$  along the Eastern Iberian margin was  $-0.70 \pm 0.54 \text{ mol m}^{-2} \text{ yr}^{-1}$ , which fall within the range of those modelled for the deep-convection area around the Bay of Marseille (Northwestern Mediterranean Basin) during 2012-2013 ( $-0.5 \text{ mol m}^{-2} \text{ yr}^{-1}$ ; Ulses et al., 2023) and estimated based on observations during 2017-2018 (between  $-0.26$  and  $-0.81 \text{ mol m}^{-2} \text{ yr}^{-1}$ ; Wimart-Rousseau et al., 2020). However, it was opposite to the net outgassing across the Eastern Mediterranean basin ( $0.85 \pm 0.27 \text{ mol m}^{-2} \text{ yr}^{-1}$  during

2009-2015; Sisma-Ventura et al., 2017). The net CO<sub>2</sub> sink for the monitored area across the Alboran Sea (14,000 Km<sup>2</sup>) and eastern Iberian margin (40,000 Km<sup>2</sup>) was  $-0.97 \pm 0.30$  Tg CO<sub>2</sub> yr<sup>-1</sup> ( $-0.26 \pm 0.08$  Tg C yr<sup>-1</sup>) and  $-1.22 \pm 0.95$  Tg CO<sub>2</sub> yr<sup>-1</sup> ( $-0.33 \pm 0.25$  Tg C yr<sup>-1</sup>). These findings powerfully contributed to the assessment of the air-sea CO<sub>2</sub> exchange in the Mediterranean basin and global coastal and shelf areas.

## 5. Conclusion

The five years of automatically underway observations at the ES-SOOP-CanOA Ocean Station provided a high spatio-temporal resolution dataset which includes the surface physical and MCS properties across the western margin of the Mediterranean Sea. It allowed the characterization, with an improved degree of certainty, of mechanisms involved in the MCS dynamics in the Alboran Sea and Eastern Iberian coastal transitional area on seasonal and interannual timescales.

The variations in  $f\text{CO}_{2,\text{sw}}$  were found to be strongly controlled by temperature fluctuations. On a seasonal scale, the thermal-driven variations intensified as AJ advanced eastward in the Alboran Sea and MAW is formed, moved northward along the eastern Iberian margin and mixed with MW. In the Alboran Sea, the high intensity of the AJ during summer warms the surface layer toward the core of the WAG and EAG, driving larger seasonal changes in SST,  $f\text{CO}_{2,\text{sw}}$  and pH which increased during the study period. The eastern Iberian margin was meridionally separated at Cape of Nao by the path of the Northern Current: the northernmost part, fed with cool, salty and remineralized MW during the cold season and influenced by the northward spreading of MAW during the warm season, show the largest seasonal amplitudes for SST,  $f\text{CO}_{2,\text{sw}}$ , and pH compared to the southernmost part, supplied with recent MAW during most of the year and by a weak and relatively warmed branch of the Northern Current during winter. The driver analysis has identified that 51-71% of the increase in  $f\text{CO}_{2,\text{sw}}$  from February to September within the entire monitored area was explained by SST and <20% by  $A_T$  and SSS, while the processes controlling  $C_T$  offset this increment, contributing by 23-37%.

The changes in the seasonal cycles were driven, in first term, by the increasing contribution of temperature (due to the seasonal amplitude of SST is becoming larger) and, in second term, by the decreasing contribution of  $C_T$  (due to the dismissing remineralization/production ratio). On an interannual scale, the SST increased at rates

ranging between 0.26 and 0.43 °C yr<sup>-1</sup> and drove a rapid increase in  $f\text{CO}_{2,\text{sw}}$  within 4.18 and 5.53  $\mu\text{atm yr}^{-1}$  and a decrease in pH within -0.0049 and -0.0065 units yr<sup>-1</sup>. The ~76-92% of the interannual increase in  $f\text{CO}_{2,\text{sw}}$  was described by warming. In the Alboran Sea and extending northward to Cape of Palos, non-thermal processes, primarily biological drawdown during spring blooms, compensated for up to one-third of the expected increase in  $f\text{CO}_{2,\text{sw}}$  due to warming. The opposite occurred north of Cape of Palos, where non-thermal processes, mainly the inflow of CO<sub>2</sub>-rich MW during the cold season, accounted for the increase in  $f\text{CO}_{2,\text{sw}}$ .

The assessment of the air-sea CO<sub>2</sub> exchange shows the Western boundary of the Mediterranean basin undersaturated and acting as a significant sink for atmospheric CO<sub>2</sub> during most of the year, while presented supersaturated conditions which led a CO<sub>2</sub> source status during the warm months. The entire monitored area acted as a net annual CO<sub>2</sub> sink, which is weakening at statistically significant rates ranging between 0.06 and 0.13 mol m<sup>-2</sup> yr<sup>-1</sup> (40-80% since 2019). These trends would lead the area to shift towards becoming a net annual CO<sub>2</sub> source before 2030 if the current climate conditions persist. The weakening in the net annual CO<sub>2</sub> sink was driven by the ongoing strength of the summer outgassing (mainly in the Alboran Sea) and the weakening in the autumn and spring ingassing (throughout the region). Integrating the annual cycle of  $f\text{CO}_2$  during the entire study period, the net CO<sub>2</sub> ingassing calculated for the Alboran Sea and Eastern Iberian Margin was  $-1.57 \pm 0.49$  and  $-0.70 \pm 0.54$  mol m<sup>-2</sup> yr<sup>-1</sup>.

This study highlights the need for systematic observation strategies to characterize the physico-chemical properties of seawater in the Mediterranean, an effort that has been required by the scientific community for the last decades. It demonstrates the effectiveness of SOOP/VOS for monitoring surface physical and biogeochemical variables, especially in highly variable and anthropogenically pressured areas such as coastal and semi-enclosed seas. The findings enhance our understanding of MSC dynamics in a key coastal transitional area of the Western Mediterranean, which is of high environmental and socio-economic importance and with implications for regional climate. Likewise, they contribute to a more accurate understanding of the role of coastal areas in the context of Global Change at both basin and global scales. Despite the relatively short study period, this research captured shifts likely driven by isolated events feedbacked by climate change, offering insights into future ocean conditions.

## **Appendix A: Data adjustments and statistical procedures**



The temporal evolution of the physico-chemical data was analysed by weekly averaging (time required by the vessel to complete a trip) at different locations along the vessel track. The average values ( $y$ ) were fitted to Eq. A.1 as a function of time (year fraction). This equation update the one used to study seasonal cycles by Curbelo-Hernández et al., (2021a; 2021b) through the addition of the  $b$  ( $year - 2019$ ) term, which provides the interannual rate of change of each seasonally-detrended variable between 2019 and 2024. The coefficients  $a-f$  and the standard errors of estimate given by Eq. A.1 for the variables considered are available in Table Sup1.

$$y = a + b (year - 2019) + c \cdot \cos(2\pi \text{ year}) + d \cdot \sin(2\pi \text{ year}) + e \cdot \cos(4\pi \text{ year}) + f \cdot \sin(4\pi \text{ year}) \quad (\text{A.1})$$

The errors in the weekly averages were determined by dividing the Standard Deviation by the square root of the number of data points used to calculate the means ( $Standard\ Deviation/\sqrt{n}$ ). The coefficient  $b$  in Eq. A.1 represented the interannual variation rates for each variable, which coincided with the slope derived from linear regressions of the detrended average values over time. The standard errors of these slopes were calculated by propagating the errors from the annual mean values.

The strength and direction of the linear regressions and the significance of the interannual trends was evaluated through the Pearson correlation test. This test yielded correlation coefficients ( $r^2$ ) and corresponding  $p$ -values to determine statistical significance. Trends with  $p$ -values  $\leq 0.01$  were statistically significant at the 99% confidence level, those with  $p$ -values  $\leq 0.05$  were significant at the 95% confidence level, and trends with  $p$ -values  $\leq 0.1$  were significant at the 90% confidence level. Trends with  $p$ -values  $> 0.1$  were not statistically significant but still provided an estimate of the temporal evolution of the variables within their respective layers.

## Appendix B: Uncertainty in FCO<sub>2</sub> explained by the propagated error in ΔfCO<sub>2</sub>

The uncertainty in ΔfCO<sub>2</sub> was calculated by applying standard error propagation rules for the difference of two independent measurements with associated uncertainties (Eq. B.1):

$$\sigma_{\Delta fCO_2} = \sqrt{\sigma_{fCO_{2,sw}}^2 + \sigma_{fCO_{2,atm}}^2} \quad \text{B.1}$$

where  $\sigma_{fCO_{2,sw}}$  and  $\sigma_{fCO_{2,atm}}$  are the uncertainties for  $fCO_{2,sw}$  and  $fCO_{2,atm}$ , respectively (see section 2.4.1). The absolute error in  $FCO_2$  ( $\sigma_{FCO_2}$ ;  $mmol\ m^{-2}\ d^{-1}$ ) associated solely with uncertainty in  $\Delta fCO_2$  was estimated for each data point using Eq. B.2:

$$\sigma_{FCO_2} = K_{660} K_0 \sigma_{\Delta fCO_2} \quad B.2$$

To represent the average magnitude of uncertainty in the estimated  $FCO_2$  over the entire dataset (with  $n$  being the total number of data), the mean absolute  $FCO_2$  error was calculated using Eq. B.3 and the mean relative  $FCO_2$  was estimated with Eq. B.4:

$$\overline{\sigma_{FCO_2}} = \frac{1}{n} \sum_{i=1}^n \sigma_{FCO_2,i} \quad B.3$$

$$\frac{\overline{\sigma_{FCO_2}}}{FCO_2} = \frac{1}{n} \sum_{i=1}^n \left| \frac{\sigma_{FCO_2,i}}{FCO_2} \right| * 100 \quad B.4$$

## Code Availability

The  $CO_{2,SYS}$  programme for MATLAB is available at <https://github.com/jonathansharp/CO2-System-Extd>.

## Data Availability Statement

The underway observations provided by the ES-SOOP-CanOA in the Western Mediterranean Sea (February 2019 – February 2024) used in this investigation are published in open-access at Zenodo ([doi.org/10.5281/zenodo.13379011](https://doi.org/10.5281/zenodo.13379011)) and available since September 2023 at the ICOS Data Portal (<https://www.icos-cp.eu/data-products/ocean-release>). The SST reanalysis monthly data ( $0.042^\circ \times 0.042^\circ$ ) from the Med MFC physical multiyear product (Escudier et al., 2020; 2021; Nigam et al., 2021) are available at Copernicus Marine Data Store (<https://data.marine.copernicus.eu/products>). ERA5 hourly wind speed reanalysis data at 10 m above the sea level used to calculate air-sea  $CO_2$  fluxes are available at Copernicus Climate Data Store (<https://cds.climate.copernicus.eu/>).

## Author contribution

All the authors made significant contributions on this research. M. G.-D., J. M. S.-C. and A.G.G. installed and maintained the equipment in the VOS. D. C-H and D. G-S participated

in routine maintenance and data acquisition. D. C.-H. developed the MATLAB® routines and conducted the data processing and analysis. All authors contributed to the writing of the manuscript and supported its submission.

**Declaration Competing interest**

The authors declare that the research was conducted in the absence of any commercial or financial relationships that could be construed as a potential conflict of interest.

**Acknowledgement**

This research was supported by the Canary Islands Government and the Loro Parque Foundation through the CanBIO project, CanOA subproject (2019–2024), and the CARBOCAN agreement (Consejería de Transición Ecológica y Energía, Gobierno de Canarias). We would like to thank the JONA SOPHIE ship owner, Reederei Stefan Patjens GmbH & Co. KG, the NISA-Marítima company and the captains and crew members for the support during this collaboration. Special thanks to the technician Adrian Castro-Álamo for biweekly equipment maintenance and discrete sampling of total alkalinity aboard the ship. We would like to thank the two anonymous reviewers for their constructive comments and suggestions, which have significantly improved the quality of this manuscript. The SOOP CanOA-VOS line is part of the Spanish contribution to the Integrated Carbon Observation System (ICOS-ERIC; <https://www.icos-cp.eu/>) since 2021 and has been recognized as an ICOS Class 1 Ocean Station. The participation of D. C-H was funded by the PhD grant PIFULPGC-2020-2 ARTHUM-2

## Legend for Figures

Figure 1. (a) Map of the Western boundary of the Mediterranean Sea with the ES-SOOP-CanOA tracks between February 2019 and February 2024 (red) and the location of the stations of interest along the southern (S1-S5) and eastern (E1-E6) sections. The main Capes and Gulf along the geographically rugged Iberian coastline are shown. The schematic diagram summarized the classical circulation patterns: in the Alboran Sea (blue), the Atlantic Jet (AJ) surrounds the Western and Eastern Anticyclonic Gyres (WAG and EAG, respectively) and forms Modified Atlantic Water (MAW), while along the Eastern Iberian margin (purple), the Mediterranean Water (MW) is transported from the Northwestern Mediterranean basin along the path of the Northern Current. The northward spreading of MAW during summer and southward spreading MW during winter is depicted with dashed arrows. The thermal front formed in the axis of the Pyrenees during summer is depicted with a black dashed line. (b) SST maps built with reanalysis monthly data ( $0.042^\circ \times 0.042^\circ$ ) for February and September 2023 from the Med MFC physical multiyear product (Escudier et al., 2020; 2021; Nigam et al., 2021), available at Copernicus Marine Data Store (<https://data.marine.copernicus.eu/products>; last access: 15 May 2025).

Figure 2. Spatial distribution of the average SST,  $f\text{CO}_{2,\text{sw}}$ , pH, and  $C_T$  calculated on a seasonal and annual basis every  $0.1^\circ$  longitude along the S section (left panels) and every  $0.25^\circ$  latitude along the E section (right panels). The 3-months periods January-March, April-June, July-September and October-December were considered as winter, spring, summer and autumn, respectively. Note the different scales used for  $C_T$  due to significant variations between the S and E sections. Standard deviations are provided in Table Sup1 and indicate the range of variability among the study period.

Figure 3. Time-series of SST,  $f\text{CO}_{2,\text{sw}}$  and pH at S1, S3 and S5 along the eastern Iberian margin within the five years of observations. The weekly average data was fitted to harmonic Eq. A.1. The thermal and non-thermal terms of the average  $f\text{CO}_{2,\text{sw}}$  calculated by following the procedures of Takahashi et al., 2002 (T'02) and Fassbender et al., 2022 (F'22) and the  $\text{pH}_{19}$  are depicted. The coefficients  $a$ - $f$ , standard errors of estimate and  $r^2$  given by Eq. A.1 are presented in Table Sup1.

Figure 4. Time-series of SST,  $f\text{CO}_{2,\text{sw}}$  and pH at E1, E4 and E5 in the Alboran Sea within the five years of observations. The weekly average data was fitted to harmonic Eq. A.1.

The thermal and non-thermal terms of the average  $f\text{CO}_{2,\text{sw}}$  calculated by following the procedures of Takahashi et al., 2002 (T,02) and Fassbender et al., 2022 (F'22) and the  $\text{pH}_{19}$  are depicted. The coefficients  $a$ - $f$ , standard errors of estimate and  $r^2$  given by Eq. A.1 are presented in Table Sup1.

Figure 5. Temporal evolution of the seasonal rates of  $f\text{CO}_{2,\text{sw}}$  explained by each of its drivers within the five years of observation. The differences between monthly average data for February and September (where minimum and maximum SST and  $f\text{CO}_{2,\text{sw}}$  were encountered) was considered to compute the seasonal trends. The standard deviation of the monthly average data was considered in the calculation of the seasonal changes and infers errors in the computation of  $f\text{CO}_{2,\text{sw}}$ , which are summarized in Table Sup3. The cumulative  $f\text{CO}_{2,\text{sw}}$  change ( $\frac{df\text{CO}_{2,\text{sw}}}{dt}$  (sum)) resulting from the distinct drivers were consistent with the observed seasonal  $f\text{CO}_{2,\text{sw}}$  trends ( $\frac{df\text{CO}_{2,\text{sw}}}{dt}$  (obs)), thereby instilling confidence in the methodology.

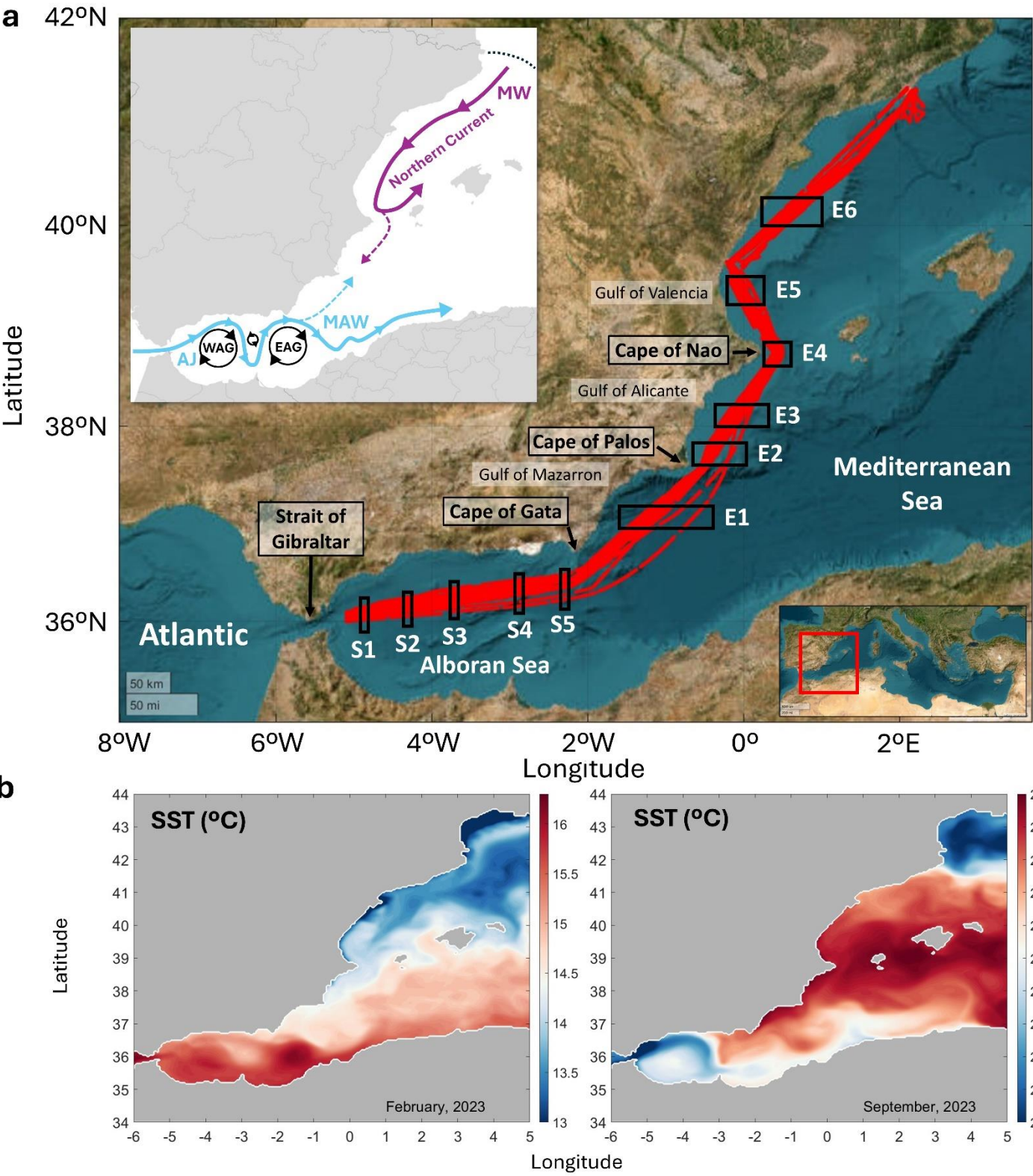
Figure 6. Temporal variations of  $\text{FCO}_2$  (blue; left axis),  $\Delta f\text{CO}_2$  (orange; right axis) and wind speed (gray; left axis) at (a) S1-S5 and (b) E1-E6. A piecewise polynomial-based smoothing spline was applied to the weekly average data (represented with dots). Gaps were covered by the harmonic fitting (Eq. A.1; dash line). The black lines represent the interannual increase in  $\text{FCO}_2$ . The seasonally-detrended interannual rates of change of  $\text{FCO}_2$  and  $\Delta f\text{CO}_2$  are shown in each panel. \*\*\* denotes that the trends are statistically significant at the 99% level of confidence, \*\* at the 95% level of confidence and \* at the 90% level of confidence. The wind speed does not show statistically significant interannual trends ( $p$ -values  $> 0.1$ ).

Figure 7. Temporal evolution of average  $\text{FCO}_2$  calculated on a seasonal and annual basis for each year (2019-2023) at S1-S5 and E1-E6. Same representation for  $\Delta f\text{CO}_2$  and wind speed is available in Figure Sup5 and Sup6. The 3-months periods January-March, April-June, July-September and October-December were considered as winter, spring, summer and autumn, respectively. The legend includes the interannual trends for  $\text{FCO}_2$  ( $\text{mol m}^{-2} \text{yr}^{-1}$ ) based on linear regression of the seasonal and annual means. \*\*\* denotes that the trends are statistically significant at the 99% level of confidence, \*\* at the 95% level of confidence and \* at the 90% level of confidence. Standard deviations are presented in Table Sup4.

## Legend for Tables

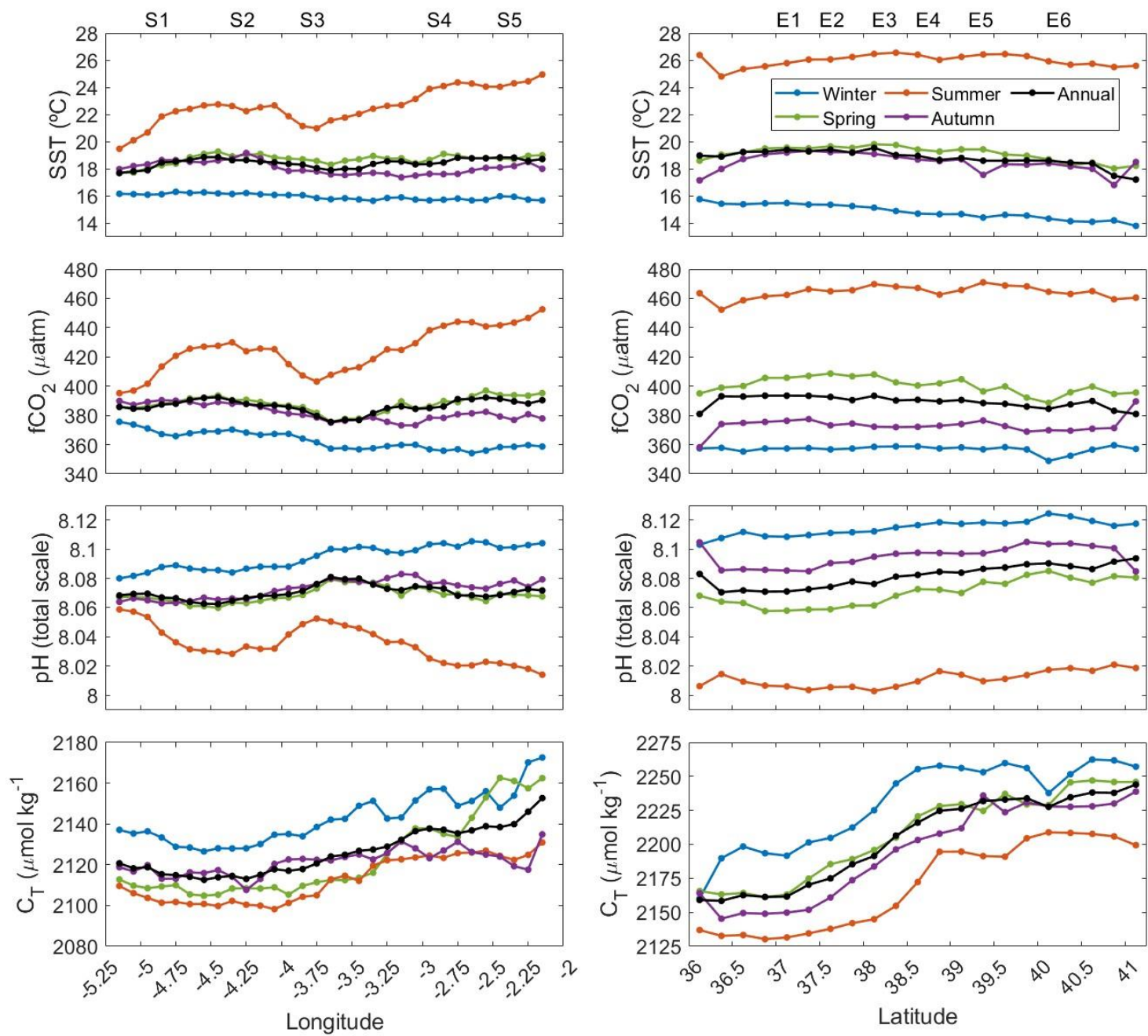
Table 1. Seasonal amplitudes and interannual trends of SST, SSS,  $f\text{CO}_{2,\text{sw}}$ , pH,  $\text{pH}_{19}$ ,  $\text{C}_\text{T}$  and  $\text{NC}_\text{T}$ . The seasonal changes were calculated as the amplitude of Eq. A.1 fitted to the weekly average data at each station. The error of the seasonal amplitudes was assumed as the product of the standard error of estimate given by the harmonic function by 2. The interannual changes were based on linear regressions and given for each station and for the entire S and E sections (considering the total amount of average data at S1-S5 and E1-E6, respectively) during the cold and warm season. The interannual trends of SST during 2000-2019 (based on reanalysis monthly data from the Med MFC physical multiyear product [Escudier et al., 2020; 2021; Nigam et al., 2021]; detailed in section 4.2) was included for comparison. The trends were obtained by the linear regressions of the seasonally-detrended weekly average data and include their standard error of estimate. \*\*\* denotes that the trends are statistically significant at the 99% level of confidence, \*\* at the 95% level of confidence and \* at the 90% level of confidence.

Table 2. Means, seasonal amplitudes and interannual rates of change of thermal and non-thermal components of  $f\text{CO}_{2,\text{sw}}$  ( $f\text{CO}_{2,\text{T}}$  and  $f\text{CO}_{2,\text{NT}}$ , respectively) calculated by following Takahashi et al., 2002 and Fassbender et al., 2022 (T'02 and F'22, respectively). The seasonal changes were calculated as the amplitude of Eq. A.1 fitted to the weekly average data at each station. The error of the seasonal amplitudes was assumed as twice the standard error of estimate given by the harmonic function. The trends were obtained by the linear regressions of the seasonally-detrended weekly average data and include their standard error of estimate. \*\*\* denotes that the trends are statistically significant at the 99% level of confidence, \*\* at the 95% level of confidence and \* at the 90% level of confidence.

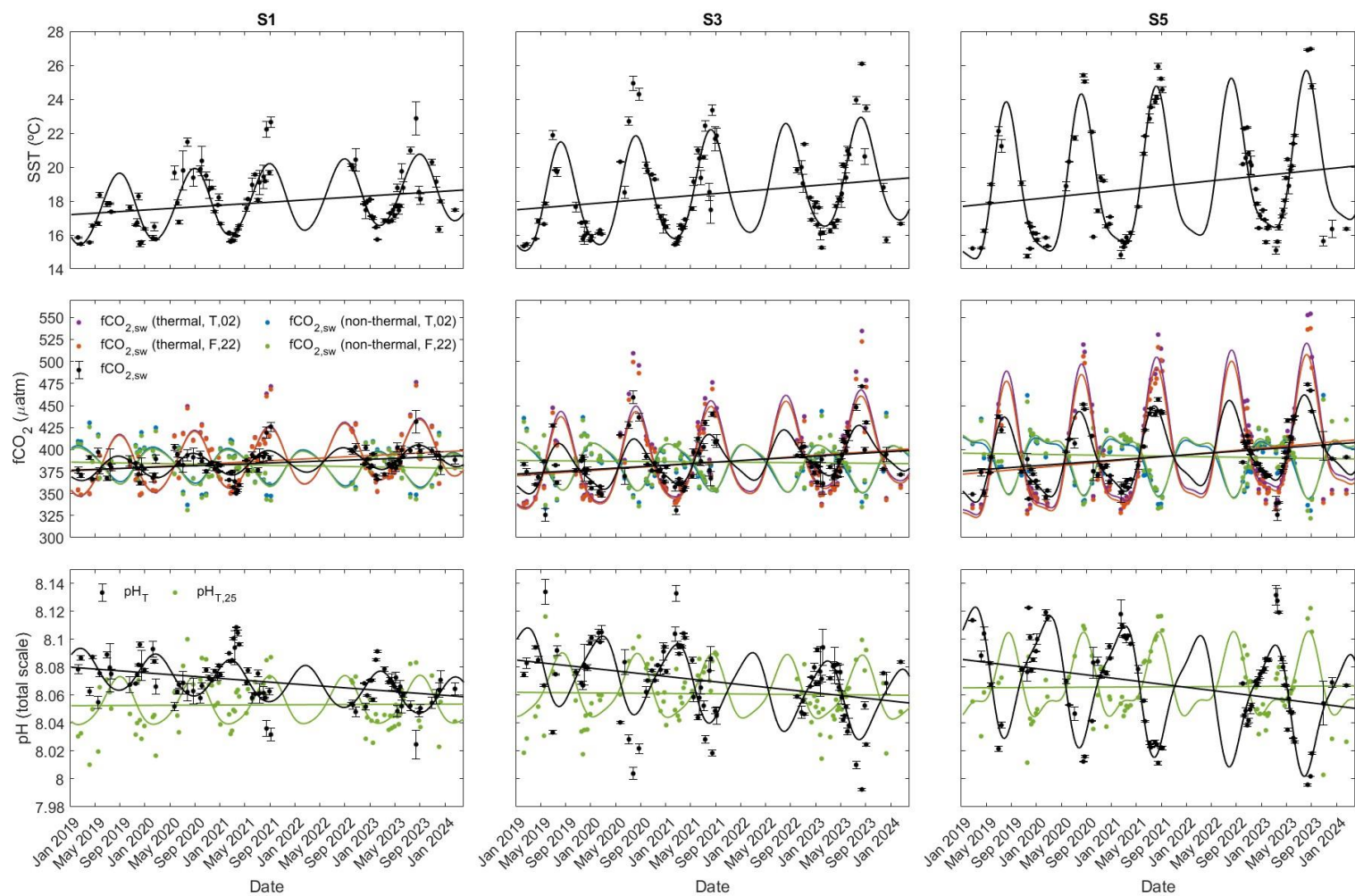


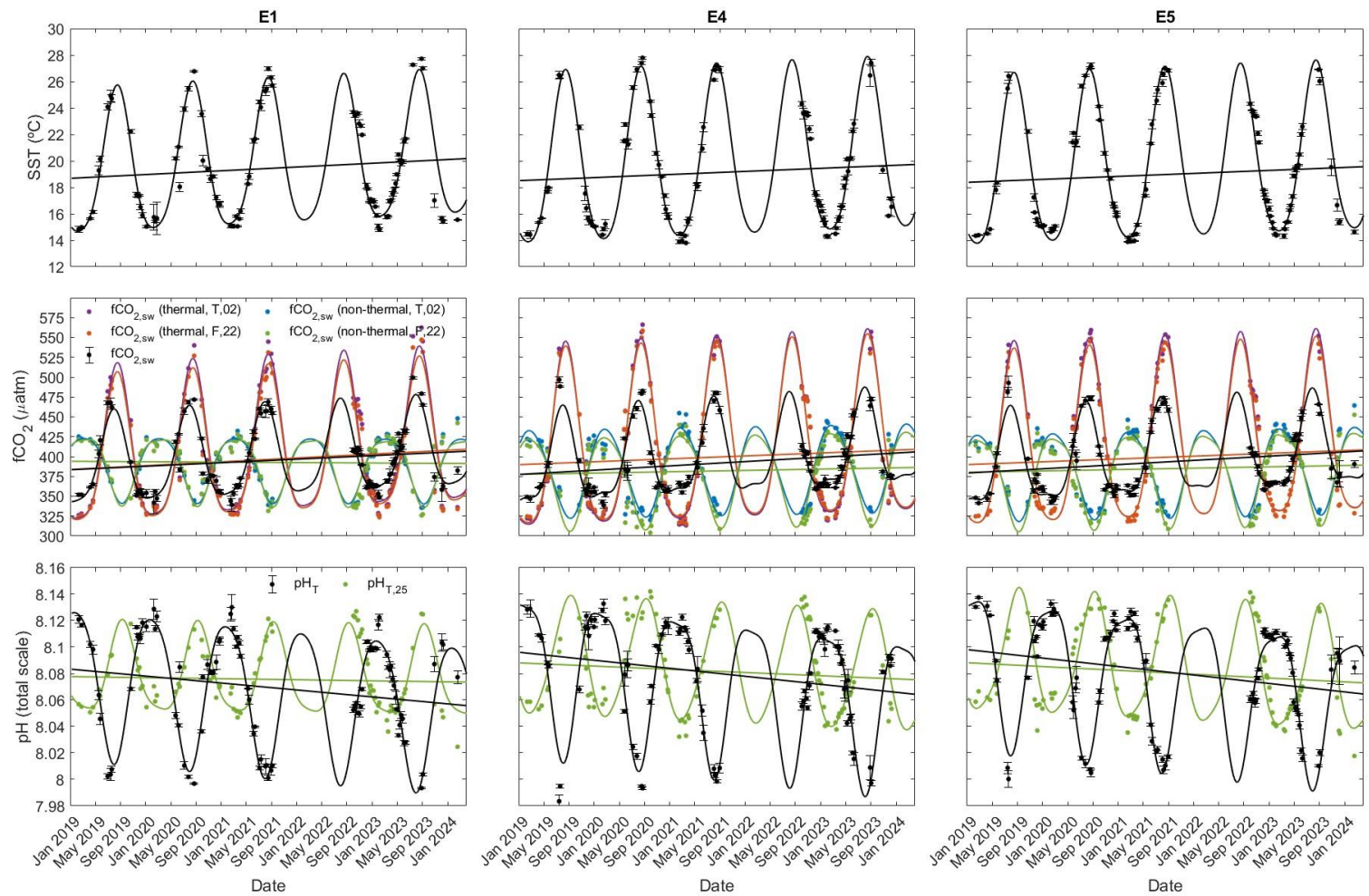


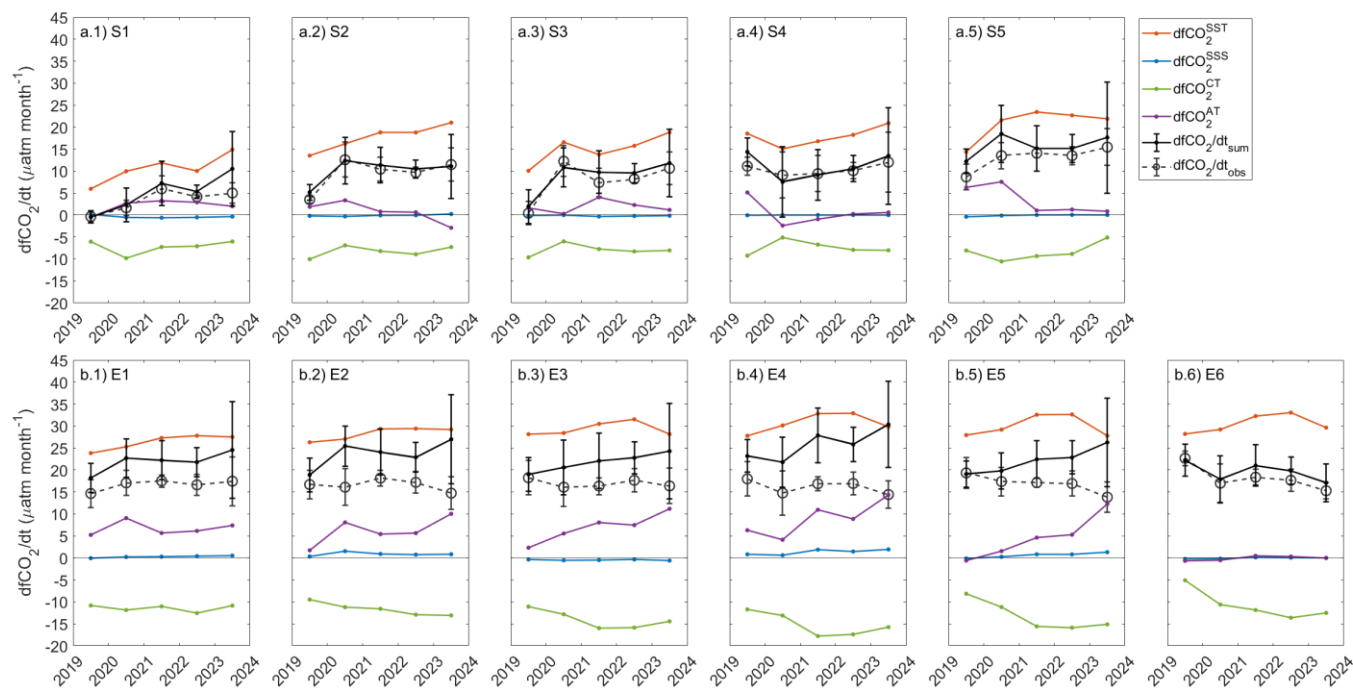
1132 Fig. 2

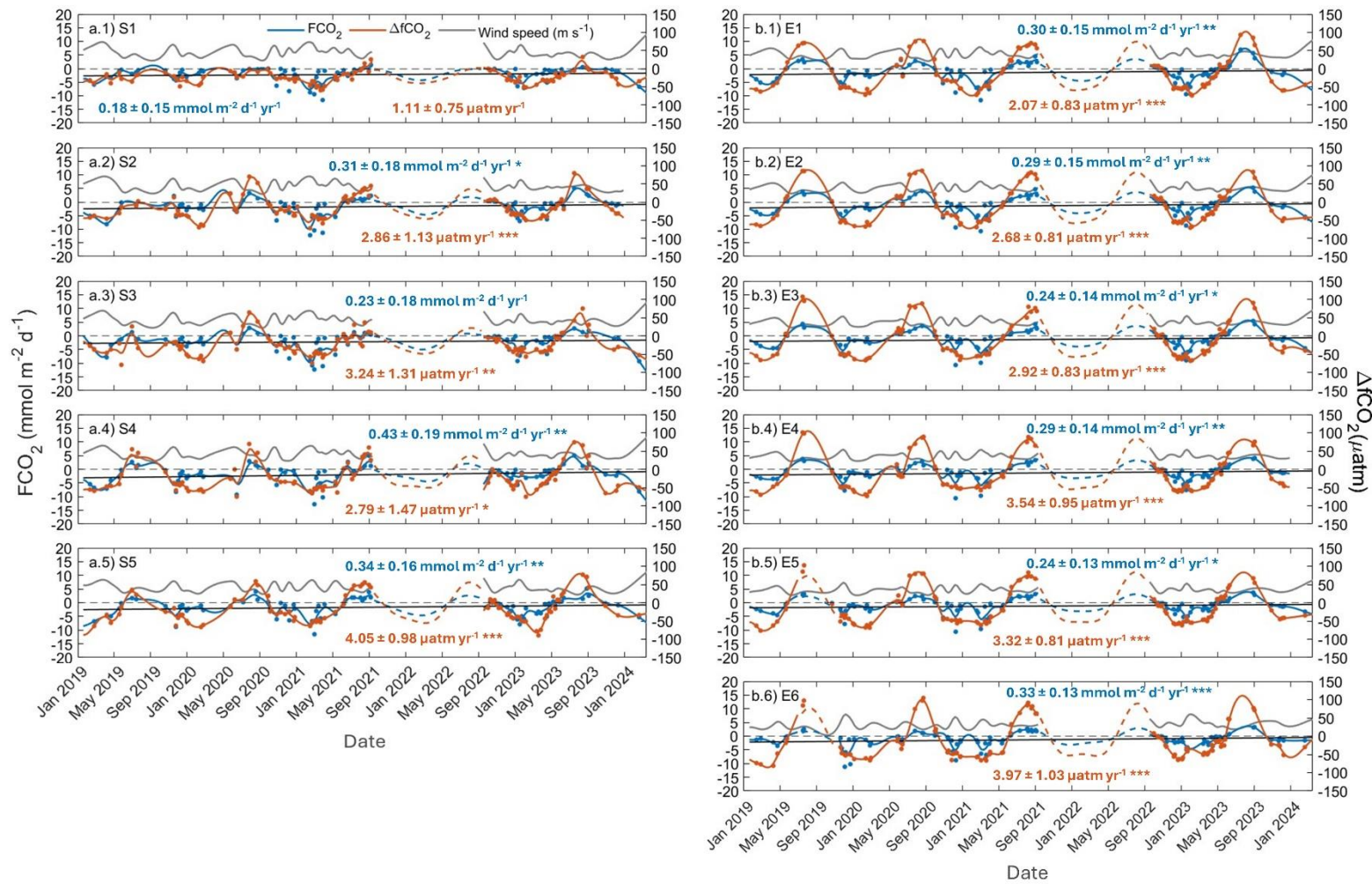




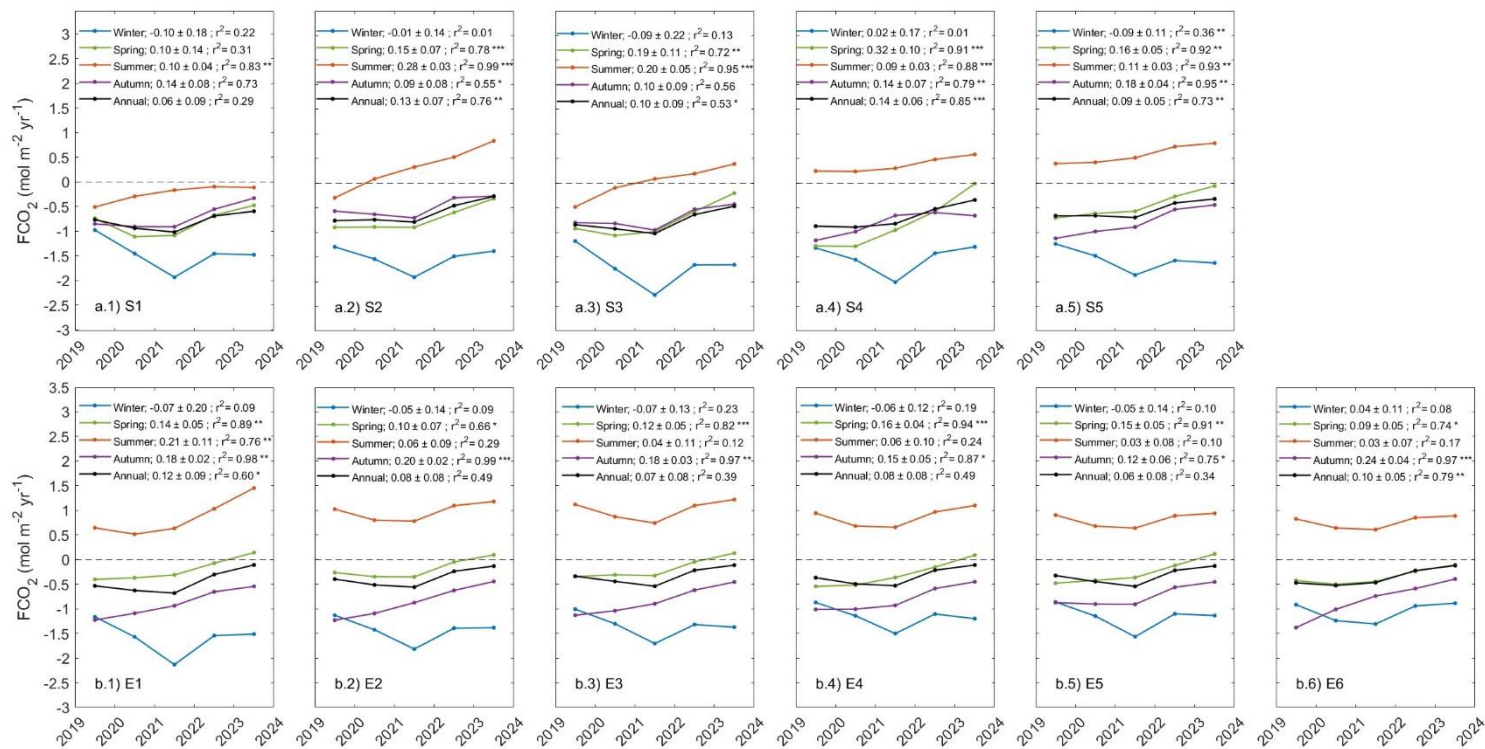












	SST		SSS		$f\text{CO}_{2,\text{sw}}$		pH		$\text{pH}_{19}$		$\text{C}_\text{T}$		$\text{NC}_\text{T}$		$\text{A}_\text{T}$		$\text{NA}_\text{T}$	
	Seasonal amplitude (°C)	Trend (°C yr <sup>-1</sup> )	Seasonal amplitude	Trend (°C yr <sup>-1</sup> )	Seasonal amplitude (µatm)	Trend (°C yr <sup>-1</sup> )	Seasonal amplitude (total scale)	Trend (°C yr <sup>-1</sup> )	Seasonal amplitude (total scale)	Trend (°C yr <sup>-1</sup> )	Seasonal amplitude (µmol kg <sup>-1</sup> )	Trend (°C yr <sup>-1</sup> )	Seasonal amplitude (µmol kg <sup>-1</sup> )	Trend (°C yr <sup>-1</sup> )	Seasonal amplitude (µmol kg <sup>-1</sup> )	Trend (°C yr <sup>-1</sup> )	Seasonal amplitude (µmol kg <sup>-1</sup> )	Trend (°C yr <sup>-1</sup> )
S1	4.21 ± 1.90	0.28 ± 0.07 ***	0.293 ± 0.328	-0.074 ± 0.012 ***	27.78 ± 20.27	3.13 ± 0.75 ***	0.0300 ± 0.0210	-0.0040 ± 0.0008 ***	0.0344 ± 0.0280	0.0002 ± 0.0010	41.2 ± 16.3	-6.4 ± 1.0 ***	26.8 ± 16.3	-2.2 ± 0.6 ***	29.4 ± 32.8	-7.4 ± 1.2 ***	10.6 ± 5.9	-2.7 ± 0.4 ***
S2	7.50 ± 2.18	0.50 ± 0.09 ***	0.158 ± 0.258	-0.078 ± 0.010 ***	70.20 ± 28.27	4.68 ± 1.10 ***	0.0674 ± 0.0254	-0.0055 ± 0.0010 ***	0.0582 ± 0.0292	0.0022 ± 0.0011 *	37.3 ± 19.4	-7.9 ± 1.1 ***	35.4 ± 19.4	-3.5 ± 0.8 ***	15.6 ± 25.9	-7.9 ± 1.0 ***	5.6 ± 4.7	-2.9 ± 0.4 ***
S3	6.42 ± 2.38	0.36 ± 0.09 ***	0.333 ± 0.334	-0.070 ± 0.012 ***	57.23 ± 35.36	5.12 ± 1.32 ***	0.0563 ± 0.0340	-0.0059 ± 0.0013 ***	0.0455 ± 0.0276	-0.0004 ± 0.0010	47.4 ± 17.6	-5.7 ± 1.1 ***	33.0 ± 17.6	-1.8 ± 0.7 ***	33.4 ± 33.7	-7.0 ± 1.3 ***	12.1 ± 6.1	-2.6 ± 0.5 ***
S4	7.53 ± 2.58	0.26 ± 0.10 ***	0.344 ± 0.457	-0.051 ± 0.017 ***	74.89 ± 38.91	4.89 ± 1.45 ***	0.0698 ± 0.0372	-0.0053 ± 0.0014 ***	0.0544 ± 0.0242	-0.0014 ± 0.0009	43.0 ± 19.9	-3.6 ± 1.6 ***	33.0 ± 19.9	-0.6 ± 0.7	34.7 ± 46.3	-5.2 ± 1.7 ***	12.5 ± 8.2	-1.9 ± 0.6 ***
S5	9.25 ± 2.34	0.45 ± 0.09 ***	0.562 ± 0.575	-0.062 ± 0.022 ***	96.99 ± 25.18	6.17 ± 0.98 ***	0.0940 ± 0.0242	-0.0067 ± 0.0009 ***	0.0601 ± 0.0304	0.0003 ± 0.0012	50.8 ± 24.3	-5.6 ± 2.0 ***	34.3 ± 24.3	-2.0 ± 0.9 ***	56.6 ± 58.0	-6.3 ± 2.2 ***	20.1 ± 10.3	-2.3 ± 0.8 ***
summer	0.59 ± 0.20 ***		-0.031 ± 0.021		7.23 ± 2.33 ***		-0.0069 ± 0.0020 ***		0.0020 ± 0.0014		-3.9 ± 1.4 ***		-2.1 ± 0.7 ***		-3.1 ± 2.2		-1.1 ± 0.8	
winter	0.26 ± 0.04 ***		-0.094 ± 0.020 ***		3.43 ± 0.96 ***		-0.0047 ± 0.0011 ***		-0.0006 ± 0.0010		-7.8 ± 1.8 ***		-2.4 ± 0.8 ***		-9.5 ± 2.0 ***		-3.4 ± 0.7 ***	
total	0.38 ± 0.05 ***		-0.065 ± 0.009 ***		4.76 ± 0.59 ***		-0.0054 ± 0.0006 ***		0.0002 ± 0.0005		-5.7 ± 0.8 ***		-2.0 ± 0.4 ***		-6.6 ± 0.9 ***		-2.4 ± 0.3 ***	
2000-2019	0.03 ± 0.00 ***																	
E1	11.07 ± 2.15	0.28 ± 0.08 ***	0.522 ± 0.463	-0.069 ± 0.017 ***	116.94 ± 23.18	4.44 ± 0.85 ***	0.1148 ± 0.0234	-0.0052 ± 0.0009 ***	0.0670 ± 0.0206	-0.0008 ± 0.0008	81.1 ± 15.1	-5.5 ± 1.4 ***	52.6 ± 15.1	-1.5 ± 0.6 ***	52.7 ± 47.0	-7.0 ± 1.7 ***	18.3 ± 8.2	-2.4 ± 0.6 ***
E2	11.64 ± 1.82	0.31 ± 0.07 ***	0.482 ± 0.486	-0.094 ± 0.018 ***	121.57 ± 21.54	4.79 ± 0.81 ***	0.1172 ± 0.0218	-0.0059 ± 0.0008 ***	0.0732 ± 0.0190	-0.0011 ± 0.0007	83.2 ± 13.5	-7.4 ± 1.5 ***	56.8 ± 13.5	-1.9 ± 0.5 ***	48.8 ± 49.2	-9.5 ± 1.9 ***	16.9 ± 8.5	-3.3 ± 0.6 ***
E3	12.44 ± 1.89	0.24 ± 0.07 ***	0.592 ± 0.604	-0.138 ± 0.023 ***	124.78 ± 21.85	4.99 ± 0.82 ***	0.1225 ± 0.0204	-0.0067 ± 0.0008 ***	0.0818 ± 0.0236	-0.0031 ± 0.0009 ***	94.1 ± 21.4	-10.2 ± 2.0 ***	63.9 ± 21.4	-2.0 ± 0.8 ***	60.0 ± 61.2	-14.0 ± 2.3 ***	20.6 ± 10.5	-4.8 ± 0.8 ***
E4	13.04 ± 1.80	0.23 ± 0.07 ***	0.768 ± 0.493	-0.068 ± 0.018 ***	120.73 ± 25.43	5.40 ± 0.94 ***	0.1196 ± 0.0234	-0.0061 ± 0.0009 ***	0.0891 ± 0.0280	-0.0024 ± 0.0010 **	120.1 ± 21.6	-4.4 ± 1.7 ***	75.1 ± 21.6	-0.4 ± 0.8	77.9 ± 49.9	-6.9 ± 1.8 ***	26.5 ± 8.5	-2.3 ± 0.6 ***
E5	12.92 ± 1.74	0.23 ± 0.06 ***	0.538 ± 0.467	-0.097 ± 0.017 ***	118.88 ± 21.72	5.31 ± 0.79 ***	0.1165 ± 0.0194	-0.0064 ± 0.0007 ***	0.0914 ± 0.0270	-0.0029 ± 0.0010 ***	98.4 ± 20.8	-6.6 ± 1.6 ***	69.3 ± 20.8	-0.9 ± 0.7	54.6 ± 47.3	-9.9 ± 1.7 ***	18.5 ± 8.0	-3.3 ± 0.6 ***
E6	13.13 ± 2.02	0.19 ± 0.07 ***	0.108 ± 0.551	-0.011 ± 0.015	124.68 ± 30.17	6.09 ± 0.99 ***	0.1159 ± 0.0256	-0.0061 ± 0.0008 ***	0.0929 ± 0.0328	-0.0032 ± 0.0011 ***	63.3 ± 27.4	0.9 ± 1.6	59.3 ± 27.4	1.6 ± 0.9	10.0 ± 54.7	-1.2 ± 1.4	3.4 ± 9.2	-0.4 ± 0.5
summer	0.29 ± 0.09 ***		-0.069 ± 0.042 *		-2.30 ± 1.02 **		0.0011 ± 0.0008		0.0037 ± 0.0012 ***		-8.5 ± 3.2 ***		-4.3 ± 0.9 ***		±	-7.0 ± 4.3	±	-2.4 ± 1.5
winter	0.20 ± 0.04 ***		-0.092 ± 0.023 ***		5.44 ± 0.41 ***		-0.0067 ± 0.0005 ***		-0.0036 ± 0.0007 ***		-5.8 ± 2.1 ***		-0.4 ± 0.8		±	-9.4 ± 2.4 ***	±	-3.2 ± 0.8 ***
total	0.30 ± 0.04 ***		-0.082 ± 0.013 ***		5.16 ± 0.37 ***		-0.0061 ± 0.0004 ***		-0.0022 ± 0.0004 ***		-5.8 ± 1.1 ***		-0.9 ± 0.4 ***		±	-8.4 ± 1.3 ***	±	-2.9 ± 0.4 ***
2000-2019	0.05 ± 0.01 ***																	



## References

- Alberola, C., Millot, C., and Font, J.: On the seasonal and mesoscale variabilities of the Northern Current during the PRIMO-0 experiment in the western Mediterranean Sea, *Oceanol. Acta*, 18, 163–192, 1995.
- Álvarez, M., Sanleón-Bartolomé, H., Tanhua, T., Mintrop, L., Luchetta, A., Cantoni, C., Schroeder, K., and Civitarese, G.: The CO<sub>2</sub> system in the Mediterranean Sea: a basin-wide perspective, *Ocean Sci.*, 10, 69–92, <https://doi.org/10.5194/os-10-69-2014>, 2014.
- Antoine, D., Chami, M., Claustre, H., d’Ortenzio, F., Morel, A., Bécu, G., Gentili, B., Louis, F., Ras, J., Roussier, E., Scott, A. J., Tailliez, D., Hooker, S. B., Guevel, P., Desté, J. F., Dempsey, C., and Adams, D.: BOUSSOLE: A joint CNRS-INSU, ESA, CNES, and NASA ocean color calibration and validation activity, *NASA Tech. Memo.*, 1–59, 2006.
- Antoine, D., d’Ortenzio, F., Hooker, S. B., Bécu, G., Gentili, B., and Tailliez, D., Scott, A. J.: Assessment of uncertainty in the ocean reflectance determined by three satellite ocean color sensors (MERIS, SeaWiFS and MODIS-A) at an offshore site in the Mediterranean Sea (BOUSSOLE project), *J. Geophys. Res. Ocean.*, 113, <https://doi.org/10.1029/2007JC004472>, 2008a.
- Antoine, D., Guevel, P., Desté, J. F., Bécu, G., Louis, F., Scott, A. J., and Bardey, P.: The “BOUSSOLE” Buoy - A new transparent-to-swell taut mooring dedicated to marine optics: Design, tests, and performance at sea, *J. Atmos. Ocean. Technol.*, 25, 968–989, <https://doi.org/10.1175/2007JTECHO563.1>, 2008b.
- Bakker, D. C. E., Alin, S. R., Bates, N., Becker, M., Gkritzalis, T., Jones, S. D., Kozyr, A., Lauvset, S. K., Metzl, N., Nakaoka, S., O’Brien, K. M., Olsen, A., Pierrot, D., Steinhoff, T., Sutton, A. J., Takao, S., Tilbrook, B., Wada, C., Wanninkhof, R., Akl, J., Arbilla, L. A., Arruda, R., Azetsu-Scott, K., Barbero, L., Beatty, C. M., Berghoff, C. F., Bittig, H. C., Burger, E. F., Campbell, K., Cardin, V., Collins, A., Coppola, L., Cronin, M., Cross, J. N., Currie, K. I., Emerson, S. R., Enright, M. P., Enyo, K., Evans, W., Feely, R. A., Flohr, A., Gehrung, M., Glockzin, M., González-Dávila, M., Hamnca, S., Hartman, S., Howden, S. D., Kam, K., Kamb, L., Körtzinger, A., Kosugi, N., Lefèvre, N., Lo Monaco, C., Macovei, V. A., Maenner Jones, S., Manalang, D., Martz, T. R., Mdokwana, B., Monacci, N. M., Monteiro, P. M. S., Mordy, C., Morell, J. M., Murata, A., Neill, C.,



1170 Noh, J.-H., Nojiri, Y., Ohman, M. D., Olivier, L., Ono, T., Petersen, W., Plueddemann,  
1171 A. J., Prytherch, J., Rehder, G., Rutgersson, A., Santana-Casiano, J. M., Schlitzer, R.,  
1172 Send, U., Skjelvan, I., Sullivan, K. F., T'Jampens, M., Tadokoro, K., Telszewski, M.,  
1173 Theetaert, H., Tsanwani, M., Vandemark, D., van Ooijen, E., Vecchia, M. H., Voynova,  
1174 Y. G., Wang, H., Weller, R. A., and Woosley, R. J.: Surface Ocean CO<sub>2</sub> Atlas Database  
1175 Version 2024 (SOCATv2024), NOAA Natl. Centers for Environ. Inf., Dataset,  
1176 <https://doi.org/10.25921/9wpm-th28>, Accessed: 15 May 2025, 2024.

1177 Bakker, D. C. E., Pfeil, B., Landa, C. S., Metzl, N., O'Brien, K. M., Olsen, A., Smith, K.,  
1178 Cosca, C., Harasawa, S., Jones, S. D., Nakaoka, S., Nojiri, Y., Schuster, U., Steinhoff, T.,  
1179 Sweeney, C., Takahashi, T., Tilbrook, B., Wada, C., Wanninkhof, R., Alin, S. R.,  
1180 Balestrini, C. F., Barbero, L., Bates, N. R., Bianchi, A. A., Bonou, F., Boutin, J., Bozec,  
1181 Y., Burger, E. F., Cai, W.-J., Castle, R. D., Chen, L., Chierici, M., Currie, K., Evans, W.,  
1182 Featherstone, C., Feely, R. A., Fransson, A., Goyet, C., Greenwood, N., Gregor, L.,  
1183 Hankin, S., Hardman-Mountford, N. J., Harlay, J., Hauck, J., Hoppema, M., Humphreys,  
1184 M. P., Hunt, C. W., Huss, B., Ibáñez, J. S. P., Johannessen, T., Keeling, R., Kitidis, V.,  
1185 Körtzinger, A., Kozyr, A., Krasakopoulou, E., Kuwata, A., Landschützer, P., Lauvset, S.  
1186 K., Lefèvre, N., Lo Monaco, C., Manke, A., Mathis, J. T., Merlivat, L., Millero, F. J.,  
1187 Monteiro, P. M. S., Munro, D. R., Murata, A., Newberger, T., Omar, A. M., Ono, T.,  
1188 Paterson, K., Pearce, D., Pierrot, D., Robbins, L. L., Saito, S., Salisbury, J., Schlitzer, R.,  
1189 Schneider, B., Schweitzer, R., Sieger, R., Skjelvan, I., Sullivan, K. F., Sutherland, S. C.,  
1190 Sutton, A. J., Tadokoro, K., Telszewski, M., Tuma, M., Van Heuven, S. M. A. C.,  
1191 Vandemark, D., Ward, B., Watson, A. J., and Xu, S.: A multi-decade record of high  
1192 quality fCO<sub>2</sub> data in version 3 of the Surface Ocean CO<sub>2</sub> Atlas (SOCAT), *Earth Syst.*  
1193 *Sci. Data*, 8, 383–413, <https://doi.org/10.5194/essd-8-383-2016>, 2016.

1194 Bates, N. R., Astor, Y. M., Church, M. J., Currie, K., Dore, J. E., González-Dávila, M.,  
1195 Lorenzoni, L., Muller-Karger, F., Olafsson, J., and Santana-Casiano, J. M.: A time-series  
1196 view of changing surface ocean chemistry due to ocean uptake of anthropogenic CO<sub>2</sub> and  
1197 ocean acidification, *Oceanography*, 27, 126–141,  
1198 <https://doi.org/10.5670/oceanog.2014.16>, 2014.

1199 Bégovic, M., and Copin-Montégut, C.: Processes controlling annual variations in the  
1200 partial pressure of CO<sub>2</sub> in surface waters of the central northwestern Mediterranean Sea

1201 (Dyfamed site), *Deep Sea Res. Part II Top. Stud. Oceanogr.*, 49, 2031–2047,  
 1202 [https://doi.org/10.1016/S0967-0645\(02\)00026-7](https://doi.org/10.1016/S0967-0645(02)00026-7), 2002.

1203 Bergamasco, A., and Malanotte-Rizzoli, P.: The circulation of the Mediterranean Sea: a  
 1204 historical review of experimental investigations, *Adv. Oceanogr. Limnol.*, 1, 11–28,  
 1205 <https://doi.org/10.1080/19475721.2010.505354>, 2010.

1206 Bolado-Penagos, M., González, C. J., Chioua, J., Sala, I., Jesús Gomiz-Pascual, J.,  
 1207 Vázquez, Á., and Bruno, M.: Submesoscale processes in the coastal margins of the Strait  
 1208 of Gibraltar. The Trafalgar – Alboran connection, *Prog. Oceanogr.*, 181, 102219,  
 1209 <https://doi.org/10.1016/j.pocean.2019.102219>, 2020.

1210 Borges, A. V., Delille, B., and Frankignoulle, M.: Budgeting sinks and sources of CO<sub>2</sub>  
 1211 in the coastal ocean: Diversity of ecosystem counts, *Geophys. Res. Lett.*, 32, 1–4,  
 1212 <https://doi.org/10.1029/2005GL023053>, 2005.

1213 Borghini, M. B. H. S., Bryden, H., Schroeder, K., Sparnocchia, S., and Vetrano, A.: The  
 1214 Mediterranean is becoming saltier, *Ocean Sci.*, 10, 693–700, [https://doi.org/10.5194/os-](https://doi.org/10.5194/os-10-693-2014)  
 1215 10-693-2014, 2014.

1216 Bormans, M., and Garrett, C.: A simple criterion for gyre formation by the surface  
 1217 outflow from a strait, with application to the Alboran Sea, *J. Geophys. Res. Ocean.*, 94,  
 1218 12,637–12,644, <https://doi.org/10.1029/JC094iC09p12637>, 1989.

1219 Bosse, A., Testor, P., Damien, P., Estournel, C., Marsaleix, P., Mortier, L., Prieur, L., and  
 1220 Taillandier, V.: Wind-forced submesoscale symmetric instability around deep convection  
 1221 in the northwestern Mediterranean Sea, *Fluids*, 6, 1–26,  
 1222 <https://doi.org/10.3390/fluids6030123>, 2021.

1223 Bourg, N., and Molcard, A.: Northern boundary current variability and mesoscale  
 1224 dynamics: a long-term HF RADAR monitoring in the North-Western Mediterranean Sea,  
 1225 *Ocean Dyn.*, 71, 851–870, <https://doi.org/10.1007/s10236-021-01466-9>, 2021.

1226 Bray, N. A., Ochoa, J., and Kinder, T. H.: The role of the interface in exchange through  
 1227 the Strait of Gibraltar, *J. Geophys. Res.*, <https://doi.org/10.1029/95JC00381>, 1995.

- 1228 Cai, W. J., Dai, M., and Wang, Y.: Air-sea exchange of carbon dioxide in ocean margins:  
1229 A province-based synthesis, *Geophys. Res. Lett.*, 33,  
1230 <https://doi.org/10.1029/2006GL026219>, 2006.
- 1231 Chen, C. T. A., Huang, T. H., Chen, Y. C., Bai, Y., He, X., and Kang, Y.: Air-sea  
1232 exchanges of CO<sub>2</sub> in the world's coastal seas, *Biogeosciences*, 10, 6509–6544,  
1233 <https://doi.org/10.5194/bg-10-6509-2013>, 2013.
- 1234 Conan, P., and Millot, C.: Variability of the northern current off Marseilles, western  
1235 Mediterranean Sea, from February to June 1992, *Oceanol. Acta*, 18, 193–205,  
1236 [https://doi.org/10.1016/0399-1784\(95\)00009-Q](https://doi.org/10.1016/0399-1784(95)00009-Q), 1995.
- 1237 Copin-Montégut, C.: Alkalinity and carbon budgets in the Mediterranean Sea, *Global*  
1238 *Biogeochem. Cycles*, 7, 915–925, <https://doi.org/10.1029/93GB01740>, 1993.
- 1239 Copin-Montégut, C., and Bégovic, M.: Distributions of carbonate properties and oxygen  
1240 along the water column (0–2000 m) in the central part of the NW Mediterranean Sea  
1241 (Dyfamed site): Influence of winter vertical mixing on air–sea CO<sub>2</sub> and O<sub>2</sub> exchanges,  
1242 *Deep Sea Res. Part II Top. Stud. Oceanogr.*, 49, 2049–2066,  
1243 [https://doi.org/10.1016/S0967-0645\(02\)00027-9](https://doi.org/10.1016/S0967-0645(02)00027-9), 2002.
- 1244 Copin-Montégut, C., Bégovic, M., and Merlivat, L.: Variability of the partial pressure of  
1245 CO<sub>2</sub> on diel to annual time scales in the Northwestern Mediterranean Sea, *Mar. Chem.*,  
1246 85, 169–189, <https://doi.org/10.1016/j.marchem.2003.10.005>, 2004.
- 1247 Coppola, L., Boutin, J., Gattuso, J. P., Lefevre, D., and Metzl, N.: The Carbonate System  
1248 in the Ligurian Sea, in: *Mediterr. Sea Era Glob. Chang. 1 30 Years Multidiscip. Study*  
1249 *Ligurian Sea*, 79–103, <https://doi.org/10.1002/9781119706960.CH4>, 2020.
- 1250 Cossarini, G., Feudale, L., Teruzzi, A., Bolzon, G., Coidessa, G., Solidoro, C., ... and  
1251 Salon, S.: High-resolution reanalysis of the Mediterranean Sea biogeochemistry (1999–  
1252 2019), *Front. Mar. Sci.*, 8, 741486, <https://doi.org/10.3389/fmars.2021.741486>, 2021.
- 1253 Cossarini, G., Lazzari, P., and Solidoro, C.: Spatiotemporal variability of alkalinity in the  
1254 Mediterranean Sea, *Biogeosciences*, 12, 1647–1658, [https://doi.org/10.5194/bg-12-1647-](https://doi.org/10.5194/bg-12-1647-2015)  
1255 2015, 2015.

1256 Curbelo-Hernández, D., González-Dávila, M., González, A. G., González-Santana, D.,  
 1257 and Santana-Casiano, J. M.: CO<sub>2</sub> fluxes in the Northeast Atlantic Ocean based on  
 1258 measurements from a surface ocean observation platform, *Sci. Total Environ.*, 775,  
 1259 145804, <https://doi.org/10.1016/j.scitotenv.2021.145804>, 2021a.

1260 Curbelo-Hernández, D., González-Dávila, M., and Santana-Casiano, J. M.: The carbonate  
 1261 system and air-sea CO<sub>2</sub> fluxes in coastal and open-ocean waters of the Macaronesia,  
 1262 *Front. Mar. Sci.*, 10:1094250. <https://doi.org/10.3389/fmars.2023.1094250>, 2023.

1263 Curbelo-Hernández, D., Pérez, F. F., González-Dávila, M., Gladyshev, S. V., González,  
 1264 A. G., González-Santana, D., Velo, A., Sokov, A., and Santana-Casiano, J. M.: Ocean  
 1265 Acidification trends and Carbonate System dynamics in the North Atlantic Subpolar Gyre  
 1266 during 2009–2019, *EGUsphere* [preprint], <https://doi.org/10.5194/egusphere-2024-1388>,  
 1267 2024.

1268 Curbelo-Hernández, D., Santana-Casiano, J. M., González, A. G., and González-Dávila,  
 1269 M.: Air-Sea CO<sub>2</sub> Exchange in the Strait of Gibraltar, *Front. Mar. Sci.*, 8, 1701,  
 1270 <https://doi.org/10.3389/FMARS.2021.745304>, 2021b.

1271 De Carlo, E. H., Mousseau, L., Passafiume, O., and Drupp, P. S., and Gattuso, J. P.:  
 1272 Carbonate Chemistry and Air-Sea CO<sub>2</sub> Flux in a NW Mediterranean Bay Over a Four-  
 1273 Year Period: 2007-2011, *Aquat. Geochemistry*, 19, 399–442,  
 1274 <https://doi.org/10.1007/s10498-013-9217-4>, 2013.

1275 de la Paz, M., Gómez-Parra, A., and Forja, J.: Seasonal variability of surface fCO<sub>2</sub> in the  
 1276 Strait of Gibraltar, *Aquat. Sci.*, 71, 55–64, <https://doi.org/10.1007/s00027-008-8060-y>,  
 1277 2009.

1278 de la Paz, M., Huertas, E. M., Padín, X. A., González-Dávila, M., Santana-Casiano, J. M.,  
 1279 Forja, J. M., Orbi, A., Pérez, F. F., and Ríos, A. F.: Reconstruction of the seasonal cycle  
 1280 of air-sea CO<sub>2</sub> fluxes in the Strait of Gibraltar, *Mar. Chem.*, 126, 155–162,  
 1281 <https://doi.org/10.1016/j.marchem.2011.05.004>, 2011.

1282 Dickson, A. G.: Standard potential of the reaction:  $\text{AgCl(s)} + 1/2\text{H}_2\text{(g)} = \text{Ag(s)} + \text{HCl(aq)}$ ,  
 1283 and the standard acidity constant of the ion  $\text{HSO}_4^-$  in synthetic sea water from 273.15 to

1284 318.15 K, J. Chem. Thermodyn., 22, 113–127, <https://doi.org/10.1016/0021->  
1285 9614(90)90074-Z, 1990.

1286 Dickson, A. G., and Goyet, C.: Handbook of methods for the analysis of the various  
1287 parameters of the carbon dioxide system in sea water, Version 2,  
1288 <https://doi.org/10.2172/10107773>, 1994.

1289 Dickson, A. G., Sabine, C. L., and Chistian, J. R.: Guide to best practices for ocean CO<sub>2</sub>  
1290 measurements, PICES Special Publ. 3:191, 2007.

1291 Dohan, K.: Journal of Geophysical Research: Oceans, J. Geophys. Res. Ocean., 122,  
1292 2647–2651, <https://doi.org/10.1002/2016JC012144>, 2017.

1293 Doney, S. C., Fabry, V. J., Feely, R. A., and Kleypas, J. A.: Ocean Acidification: The  
1294 Other CO<sub>2</sub> Problem, Ann. Rev. Mar. Sci., 1, 169–192,  
1295 <https://doi.org/10.1146/annurev.marine.010908.163834>, 2009.

1296 D’Ortenzio, F., Antoine, D., and Marullo, S.: Satellite-driven modeling of the upper ocean  
1297 mixed layer and air-sea CO<sub>2</sub> flux in the Mediterranean Sea, Deep Sea Res. Part I  
1298 Oceanogr. Res. Pap., 55, 405–434, <https://doi.org/10.1016/j.dsr.2007.12.008>, 2008.

1299 Echevarría, F., García Lafuente, J., Bruno, M., Gorsky, G., Goutx, M., González, N.,  
1300 García, C. M., Gómez, F., Vargas, J. M., Picheral, M., Striby, L., Varela, M., Alonso, J.  
1301 J., Reul, A., Cózar, A., Prieto, L., Sarhan, T., Plaza, F., and Jiménez-Gómez, F.: Physical-  
1302 biological coupling in the Strait of Gibraltar, Deep Sea Res. Part II Top. Stud. Oceanogr.,  
1303 49, 4115–4130, [https://doi.org/10.1016/S0967-0645\(02\)00145-5](https://doi.org/10.1016/S0967-0645(02)00145-5), 2002.

1304 Escudier, R., Clementi, E., Omar, M., Cipollone, A., Pistoia, J., Aydogdu, A., Drudi, M.,  
1305 Grandi, A., Lyubartsev, V., Lecci, R., Cretí, S., Masina, S., Coppini, G., and Pinardi, N.:  
1306 Mediterranean Sea Physical Reanalysis (CMEMS MED-Currents) (Version 1) [Data set],  
1307 Copernicus Monitoring Environment Marine Service (CMEMS),  
1308 [https://doi.org/10.25423/CMCC/MEDSEA\\_MULTIYEAR\\_PHY\\_006\\_004\\_E3R1](https://doi.org/10.25423/CMCC/MEDSEA_MULTIYEAR_PHY_006_004_E3R1),  
1309 2020.

1310 Escudier, R., Clementi, E., Cipollone, A., Pistoia, J., Drudi, M., Grandi, A., Lyubartsev,  
1311 V., Lecci, R., Aydogdu, A., Delrosso, D., Omar, M., Masina, S., Coppini, G., and Pinardi,

1312 N.: A High Resolution Reanalysis for the Mediterranean Sea, *Front. Earth Sci.*, 9, 1060,  
 1313 <https://doi.org/10.3389/feart.2021.702285>, 2021.

1314 Fassbender, A. J., Schlunegger, S., Rodgers, K. B., and Dunne, J. P.: Quantifying the Role  
 1315 of Seasonality in the Marine Carbon Cycle Feedback: An ESM2M Case Study, *Global*  
 1316 *Biogeochem. Cycles*, 36, 1–15, <https://doi.org/10.1029/2021GB007018>, 2022.

1317 Folkard, A. M., Davies, P. A., Fiúza, A. F. G., and Ambar, I.: Remotely sensed sea surface  
 1318 thermal patterns in the Gulf of Cadiz and the Strait of Gibraltar: Variability, correlations,  
 1319 and relationships with the surface wind field, *J. Geophys. Res. Ocean.*, 102, 5669–5683,  
 1320 <https://doi.org/10.1029/96JC02505>, 1997.

1321 Ford, D. J., Tilstone, G. H., Shutler, J. D., and Kitidis, V.: Identifying the biological  
 1322 control of the annual and multi-year variations in South Atlantic air-sea CO<sub>2</sub> flux,  
 1323 *Biogeosciences*, 19, 4287–4304, <https://doi.org/10.5194/bg-19-4287-2022>, 2022.

1324 Frankignoulle, M., and Borges, A. V.: European continental shelf as a significant sink for  
 1325 atmospheric carbon dioxide, *Global Biogeochem. Cycles*, 15, 569–576,  
 1326 <https://doi.org/10.1029/2000GB001307>, 2001.

1327 Friedlingstein, P., O'Sullivan, M., Jones, M. W., Andrew, R. M., Bakker, D. C. E., Hauck,  
 1328 J., Landschützer, P., Le Quéré, C., Luijkx, I. T., Peters, G. P., Peters, W., Pongratz, J.,  
 1329 Schwingshackl, C., Sitch, S., Canadell, J. G., Ciais, P., Jackson, R. B., Alin, S. R.,  
 1330 Anthoni, P., Barbero, L., Bates, N. R., Becker, M., Bellouin, N., Decharme, B., Bopp, L.,  
 1331 Brasika, I. B. M., Cadule, P., Chamberlain, M. A., Chandra, N., Chau, T.-T.-T.,  
 1332 Chevallier, F., Chini, L. P., Cronin, M., Dou, X., Enyo, K., Evans, W., Falk, S., Feely, R.  
 1333 A., Feng, L., Ford, D. J., Gasser, T., Ghattas, J., Gkritzalis, T., Grassi, G., Gregor, L.,  
 1334 Gruber, N., Gürses, Ö., Harris, I., Hefner, M., Heinke, J., Houghton, R. A., Hurtt, G. C.,  
 1335 Iida, Y., Ilyina, T., Jacobson, A. R., Jain, A., Jarníková, T., Jersild, A., Jiang, F., Jin, Z.,  
 1336 Joos, F., Kato, E., Keeling, R. F., Kennedy, D., Klein Goldewijk, K., Knauer, J.,  
 1337 Korsbakken, J. I., Körtzinger, A., Lan, X., Lefèvre, N., Li, H., Liu, J., Liu, Z., Ma, L.,  
 1338 Marland, G., Mayot, N., McGuire, P. C., McKinley, G. A., Meyer, G., Morgan, E. J.,  
 1339 Munro, D. R., Nakaoka, S.-I., Niwa, Y., O'Brien, K. M., Olsen, A., Omar, A. M., Ono,  
 1340 T., Paulsen, M., Pierrot, D., Pocock, K., Poulter, B., Powis, C. M., Rehder, G., Resplandy,  
 1341 L., Robertson, E., Rödenbeck, C., Rosan, T. M., Schwinger, J., Séférian, R., Smallman,

1342 T. L., Smith, S. M., Sospedra-Alfonso, R., Sun, Q., Sutton, A. J., Sweeney, C., Takao, S.,  
 1343 Tans, P. P., Tian, H., Tilbrook, B., Tsujino, H., Tubiello, F., van der Werf, G. R., van  
 1344 Ooijen, E., Wanninkhof, R., Watanabe, M., Wimart-Rousseau, C., Yang, D., Yang, X.,  
 1345 Yuan, W., Yue, X., Zaehle, S., Zeng, J., and Zheng, B.: Global Carbon Budget 2023,  
 1346 Earth Syst. Sci. Data, 15, 5301–5369, <https://doi.org/10.5194/essd-15-5301-2023>, 2023.

1347 Fröb, F., Olsen, A., Becker, M., Chafik, L., Johannessen, T., Reverdin, G., and Omar, A.:  
 1348 Wintertime fCO<sub>2</sub> Variability in the Subpolar North Atlantic Since 2004, Geophys. Res.  
 1349 Lett., 46, 1580–1590, <https://doi.org/10.1029/2018GL080554>, 2019.

1350 Frölicher, T. L., Fischer, E. M., and Gruber, N.: Marine heatwaves under global warming,  
 1351 Nature, 560, 360–364, <https://doi.org/10.1038/s41586-018-0383-9>, 2018.

1352 García-Ibáñez, M. I., Zunino, P., Fröb, F., Carracedo, L. I., Ríos, A. F., Mercier, H.,  
 1353 Olsen, A., and Pérez, F. F.: Ocean acidification in the subpolar North Atlantic: Rates and  
 1354 mechanisms controlling pH changes, Biogeosciences, 13, 3701–3715,  
 1355 <https://doi.org/10.5194/bg-13-3701-2016>, 2016.

1356 García Lafuente, J., Álvarez Fanjul, E., Vargas, J. M., and Ratsimandresy, A. W.:  
 1357 Subinertial variability in the flow through the Strait of Gibraltar, J. Geophys. Res. Ocean.,  
 1358 107, 1–9, <https://doi.org/10.1029/2001jc001104>, 2002.

1359 Gómez-Jakobsen, F. J., Mercado, J. M., Cortés, D., and Yebra, L., Salles, S.: A first  
 1360 description of the summer upwelling off the Bay of Algeciras and its role in the  
 1361 northwestern Alboran Sea, Estuar. Coast. Shelf Sci., 225, 106230,  
 1362 <https://doi.org/10.1016/j.ecss.2019.05.012>, 2019.

1363 González-Dávila, M., and Santana-Casiano, J. M.: Long-term trends of pH and inorganic  
 1364 carbon in the Eastern North Atlantic: the ESTOC site, Front. Mar. Sci., 10, 1–16,  
 1365 <https://doi.org/10.3389/fmars.2023.1236214>, 2023.

1366 Hersbach, H., Bell, B., Berrisford, P., Biavati, G., Horányi, A., Muñoz Sabater, J.,  
 1367 Nicolas, J., Peubey, C., Radu, R., Rozum, I., Schepers, D., Simmons, A., Soci, C., Dee,  
 1368 D., and Thépaut, J.-N.: ERA5 hourly data on single levels from 1940 to present,  
 1369 Copernicus Climate Change Service (C3S) Climate Data Store (CDS),  
 1370 <https://doi.org/10.24381/cds.adbb2d47>, 2023.

1371 Hoegh-Guldberg, O., Cai, R., Poloczanska, E. S., Brewer, P. G., Sundby, S., Hilmi, K.,  
 1372 Fabry, V. J., and Jung, S.: The Ocean, in: *Climate Change 2014: Impacts, Adaptation,*  
 1373 *and Vulnerability. Part B: Regional Aspects, Contribution of Working Group II to the*  
 1374 *Fifth Assessment Report of the Intergovernmental Panel on Climate Change*, edited by:  
 1375 V. R. Barros, C. B. Field, D. J. Dokken, M. D. Mastrandrea, K. J. Mach, T. E. Bilir, M.  
 1376 Chatterjee, K. L. Ebi, Y. O. Estrada, R. C. Genova, B. Girma, E. S. Kissel, A. N. Levy,  
 1377 S. MacCracken, P. R. Mastrandrea, and L. L. White, Cambridge Univ. Press, Cambridge,  
 1378 UK and New York, NY, USA, 1655–1731, 2014.

1379 Hoegh-Guldberg, O., Jacob, D., Taylor, M., Bindi, M., Brown, S., Camilloni, I.,  
 1380 Diedhiou, A., Djalante, R., Ebi, K. L., Engelbrecht, F., Guiot, J., Hijioka, Y., Mehrotra,  
 1381 S., Payne, A., S. I. Seneviratne, A. Thomas, R. Warren, and G. Zhou: Impacts of 1.5°C  
 1382 Global Warming on Natural and Human Systems, in: *Global Warming of 1.5°C: An IPCC*  
 1383 *Special Report on the Impacts of Global Warming of 1.5°C Above Pre-Industrial Levels*  
 1384 *and Related Global Greenhouse Gas Emission Pathways*, edited by: V. Masson-Delmotte,  
 1385 P. Zhai, H.-O. Pörtner, D. Roberts, J. Skea, P. R. Shukla, A. Pirani, W. Moufouma-Okia,  
 1386 C. Péan, R. Pidcock, S. Connors, J. B. R. Matthews, Y. Chen, X. Zhou, M. I. Gomis, E.  
 1387 Lonnoy, T. Maycock, M. Tignor, and T. Waterfield, Cambridge Univ. Press, Cambridge,  
 1388 UK and New York, NY, USA, 175–312, <https://doi.org/10.1017/9781009157940.005>,  
 1389 2018.

1390 Hood, E. M., and Merlivat, L.: Annual to interannual variations of fCO<sub>2</sub> in the  
 1391 northwestern Mediterranean Sea: Results from hourly measurements made by CARIOCA  
 1392 buoys, 1995-1997, *J. Mar. Res.*, 59, 113–131,  
 1393 <https://doi.org/10.1357/002224001321237399>, 2001.

1394 IPCC: *Climate Change 2023: Synthesis Report, Contribution of Working Groups I, II and*  
 1395 *III to the Sixth Assessment Report of the Intergovernmental Panel on Climate Change*,  
 1396 edited by: H. Lee and J. Romero, IPCC, Geneva, Switzerland, 35–115,  
 1397 <https://doi.org/10.59327/IPCC/AR6-9789291691647>, 2023.

1398 Jiang, Z. P., Tyrrell, T., Hydes, D. J., Dai, M., and Hartman, S. E.: Variability of alkalinity  
 1399 and the alkalinity–salinity relationship in the tropical and subtropical surface ocean,  
 1400 *Global Biogeochem. Cycles*, 28(7), 729–742, <https://doi.org/10.1002/2013GB004678>.  
 1401 2014.



- 1402 Johnson, K. M., Wills, K. D., Butler, D. B., Johnson, W. K., and Wong, C. S.:  
 1403 Coulometric total carbon dioxide analysis for marine studies: maximizing the  
 1404 performance of an automated gas extraction system and coulometric detector, *Mar.*  
 1405 *Chem.*, 44, 167–187, [https://doi.org/10.1016/0304-4203\(93\)90201-X](https://doi.org/10.1016/0304-4203(93)90201-X), 1993.
- 1406 Lacombe, H., and Richez, C.: The regime of the strait of Gibraltar, *Elsevier Oceanogr.*  
 1407 *Ser.*, 34, 13–73, [https://doi.org/10.1016/S0422-9894\(08\)71237-6](https://doi.org/10.1016/S0422-9894(08)71237-6), 1982.
- 1408 Lee, K., Kim, T. W., Byrne, R. H., Millero, F. J., Feely, R. A., and Liu, Y. M.: The  
 1409 universal ratio of boron to chlorinity for the North Pacific and North Atlantic oceans,  
 1410 *Geochim. Cosmochim. Acta*, 74, 1801–1811, <https://doi.org/10.1016/j.gca.2009.12.027>,  
 1411 2010.
- 1412 Lee, K., Tong, L. T., Millero, F. J., Sabine, C. L., Dickson, A. G., Goyet, C., Park, G. H.,  
 1413 Wanninkhof, R., Feely, R. A., and Key, R. M.: Global relationships of total alkalinity  
 1414 with salinity and temperature in surface waters of the world’s oceans, *Geophys. Res. Lett.*,  
 1415 33, 1–5, <https://doi.org/10.1029/2006GL027207>, 2006.
- 1416 Lewis, E., and Wallace, D.: Program Developed for CO<sub>2</sub> System Calculations  
 1417 ORNL/CDIAC-105, Carbon Dioxide Information Analysis Centre, 1998.
- 1418 López-García, M.J., Millot, C., Font, J., and García-Ladona, E.: Surface circulation  
 1419 variability in the Balearic Basin, *J. Geophys. Res.*, 99, 3285–3296,  
 1420 <https://doi.org/10.1029/93JC02114>, 1994.
- 1421 Lovenduski, N.S., Gruber, N., Doney, S.C., and Lima, I.D.: Enhanced CO<sub>2</sub> outgassing in  
 1422 the Southern Ocean from a positive phase of the Southern Annular Mode, *Global*  
 1423 *Biogeochem. Cycles*, 21, 1–14, <https://doi.org/10.1029/2006GB002900>, 2007.
- 1424 Lueker, T.J., Dickson, A.G., and Keeling, C.D.: Ocean pCO<sub>2</sub> calculated from dissolved  
 1425 inorganic carbon, alkalinity, and equations for K<sub>1</sub> and K<sub>2</sub>: Validation based on laboratory  
 1426 measurements of CO<sub>2</sub> in gas and seawater at equilibrium, *Mar. Chem.*, 70, 105–119,  
 1427 [https://doi.org/10.1016/S0304-4203\(00\)00022-0](https://doi.org/10.1016/S0304-4203(00)00022-0), 2000.
- 1428 Macías, D., Bruno, M., Echevarría, F., Vázquez, A., and García, C.M.: Meteorologically-  
 1429 induced mesoscale variability of the North-western Alboran Sea (southern Spain) and

- 1430 related biological patterns, *Estuar. Coast. Shelf Sci.*, 78, 250–266,  
1431 <https://doi.org/10.1016/j.ecss.2007.12.008>, 2008.
- 1432 Macias, D., Garcia-Goriz, E., and Stips, A.: The seasonal cycle of the Atlantic Jet  
1433 dynamics in the Alboran Sea: Direct atmospheric forcing versus Mediterranean  
1434 thermohaline circulation, *Ocean Dyn.*, 66, 137–151, [https://doi.org/10.1007/s10236-015-](https://doi.org/10.1007/s10236-015-0914-y)  
1435 0914-y, 2016.
- 1436 Marcellin Yao, K., Marcou, O., Goyet, C., Guglielmi, V., Touratier, F., and Savy, J.P.:  
1437 Time variability of the north-western Mediterranean Sea pH over 1995–2011, *Mar.*  
1438 *Environ. Res.*, 116, 51–60, <https://doi.org/10.1016/J.MARENVRES.2016.02.016>, 2016.
- 1439 Marty, J.C.: The DYFAMED time-series program (French-JGOFS), *Deep-Sea Res. Part*  
1440 *II Top. Stud. Oceanogr.*, 49, 1963–1964, [https://doi.org/10.1016/S0967-0645\(02\)00021-](https://doi.org/10.1016/S0967-0645(02)00021-8)  
1441 8, 2002.
- 1442 Mémery, L., Lévy, M., Vérant, S., and Merlivat, L.: The relevant time scales in estimating  
1443 the air-sea CO<sub>2</sub> exchange in a mid-latitude region, *Deep-Sea Res. Part II Top. Stud.*  
1444 *Oceanogr.*, 49, 2067–2092, [https://doi.org/10.1016/S0967-0645\(02\)00028-0](https://doi.org/10.1016/S0967-0645(02)00028-0), 2002.
- 1445 Merlivat, L., Boutin, J., Antoine, D., Beaumont, L., Golbol, M., and Vellucci, V.: Increase  
1446 of dissolved inorganic carbon and decrease in pH in near-surface waters in the  
1447 Mediterranean Sea during the past two decades, *Biogeosciences*, 15, 5653–5662,  
1448 <https://doi.org/10.5194/bg-15-5653-2018>, 2018.
- 1449 Millero, F.J., Zhang, J., Lee, K., and Campbell, D.M.: Titration alkalinity of seawater,  
1450 *Mar. Chem.*, 44, 153–165, [https://doi.org/10.1016/0304-4203\(93\)90009-R](https://doi.org/10.1016/0304-4203(93)90009-R), 1993.
- 1451 Millero, F. J., Morse, J., and Chen, C. T.: The carbonate system in the western  
1452 Mediterranean Sea, *Deep-Sea Res. Part A Oceanogr. Res. Pap.*, 26, 1395–1404,  
1453 [https://doi.org/10.1016/0198-0149\(79\)90064-2](https://doi.org/10.1016/0198-0149(79)90064-2), 1979.
- 1454 Millot, C.: Circulation in the Western Mediterranean Sea, *J. Mar. Syst.*, 20, 423–442,  
1455 [https://doi.org/10.1016/S0924-7963\(98\)00078-5](https://doi.org/10.1016/S0924-7963(98)00078-5), 1999.
- 1456 Millot, C., and Taupier-Letage, I.: Circulation in the Mediterranean Sea, in: *The*  
1457 *Mediterranean Sea*, edited by: S. G. *The Mediterranean Sea*, 29–66, 2005.

1458 Minas, H.J., Coste, B., Le Corre, P., Minas, M., and Raimbault, P.: Biological and  
 1459 geochemical signatures associated with the water circulation through the Strait of  
 1460 Gibraltar and in the western Alboran Sea, *J. Geophys. Res.*, 96, 8755–8771,  
 1461 <https://doi.org/10.1029/91JC00360>, 1991.

1462 Mintrop, L., Pérez, F.F., González-Dávila, M., Santana-Casiano, J.M., and Körtzinger,  
 1463 A.: Alkalinity determination by potentiometry: Intercalibration using three different  
 1464 methods, *Ciencias Mar.*, 26, 23–37, <https://doi.org/10.7773/cm.v26i1.573>, 2000.

1465 Nielsen, J. N.: Hydrography of the Mediterranean and adjacent seas, *Danish Oceanogr.*  
 1466 *Exped.*, 1908–10, Report I, 72–191, 1912.

1467 Nigam, T., Escudier, R., Pistoia, J., Aydogdu, A., Omar, M., Clementi, E., Cipollone, A.,  
 1468 Drudi, M., Grandi, A., Mariani, A., Lyubartsev, V., Lecci, R., Cretí, S., Masina, S.,  
 1469 Coppini, G., and Pinardi, N.: Mediterranean Sea Physical Reanalysis INTERIM  
 1470 (CMEMS MED-Currents, E3R1i system) (Version 1) [Data set], Copernicus Monitoring  
 1471 Environment Marine Service (CMEMS),  
 1472 [https://doi.org/10.25423/CMCC/MEDSEA\\_MULTIYEAR\\_PHY\\_006\\_004\\_E3R1I](https://doi.org/10.25423/CMCC/MEDSEA_MULTIYEAR_PHY_006_004_E3R1I),  
 1473 2021.

1474 Oliver, E.C.J., Donat, M.G., Burrows, M.T., Moore, P.J., Smale, D.A., Alexander, L.V.,  
 1475 Benthuyssen, J.A., Feng, M., Sen Gupta, A., Hobday, A.J., Holbrook, N.J., Perkins-  
 1476 Kirkpatrick, S.E., Scannell, H.A., Straub, S.C., and Wernberg, T.: Longer and more  
 1477 frequent marine heatwaves over the past century, *Nat. Commun.*, 9, 1–12,  
 1478 <https://doi.org/10.1038/s41467-018-03732-9>, 2018.

1479 Orr, J. C., Epitalon, J.-M., Dickson, A. G., and Gattuso, J.-P.: Routine uncertainty  
 1480 propagation for the marine carbon dioxide system, *Mar. Chem.*, 207, 84–107,  
 1481 <https://doi.org/10.1016/j.marchem.2018.10.006>, 2018.

1482 Padin, X.A., Vazquez-Rodriguez, M., Castaño, M., Velo, A., Alonso-Perez, F., Gago, J.,  
 1483 Gilcoto, M., Alvarez, M., Pardo, P.C., De La Paz, M., Rios, A.F., and Pérez, F.F.: Air-  
 1484 Sea CO<sub>2</sub> fluxes in the Atlantic as measured during boreal spring and autumn,  
 1485 *Biogeosciences*, 7, 1587–1606, <https://doi.org/10.5194/bg-7-1587-2010>, 2010.

1486 Palmiéri, J., Orr, J.C., Dutay, J.-C., Béranger, K., Schneider, A., Beuvier, J., and Somot,  
 1487 S.: Simulated anthropogenic CO<sub>2</sub> storage and acidification of the Mediterranean Sea,  
 1488 Biogeosciences, 12, 781–802, <https://doi.org/10.5194/bg-12-781-2015>, 2015a.

1489 Palmiéri, J., Orr, J.C., Dutay, J.C., Béranger, K., Schneider, A., Beuvier, J., and Somot,  
 1490 S.: Simulated anthropogenic CO<sub>2</sub> storage and acidification of the Mediterranean Sea,  
 1491 Biogeosciences, 12, 781–802, <https://doi.org/10.5194/bg-12-781-2015>, 2015b.

1492 Peliz, A., Boutov, D., and Teles-Machado, A.: The Alboran Sea mesoscale in a long term  
 1493 high resolution simulation: Statistical analysis, Ocean Model., 72, 32–52,  
 1494 <https://doi.org/10.1016/j.ocemod.2013.07.002>, 2013.

1495 Peliz, Á., Teles-Machado, A., Marchesiello, P., Dubert, J., and Lafuente, J.G.: Filament  
 1496 generation off the Strait of Gibraltar in response to gap winds, Dyn. Atmos. Ocean., 46,  
 1497 36–45, <https://doi.org/10.1016/j.dynatmoce.2008.08.002>, 2009.

1498 Pérez, F.F., and Fraga, F.: Association constant of fluoride and hydrogen ions in seawater,  
 1499 Mar. Chem., 21, 161–168, [https://doi.org/10.1016/0304-4203\(87\)90036-3](https://doi.org/10.1016/0304-4203(87)90036-3), 1987.

1500 Pérez, F.F., Olafsson, J., Ólafsdóttir, S.R., Fontela, M., and Takahashi, T.: Contrasting  
 1501 drivers and trends of ocean acidification in the subarctic Atlantic, Sci. Rep., 11, 1–16,  
 1502 <https://doi.org/10.1038/s41598-021-93324-3>, 2021.

1503 Pierrot, D., Neill, C., Sullivan, K., Castle, R., Wanninkhof, R., Lüger, H., Johannessen,  
 1504 T., Olsen, A., Feely, R.A., and Cosca, C.E.: Recommendations for autonomous underway  
 1505 pCO<sub>2</sub> measuring systems and data-reduction routines, Deep-Sea Res. Part II Top. Stud.  
 1506 Oceanogr., 56, 512–522, <https://doi.org/10.1016/j.dsr2.2008.05.014>, 2009.

1507 Pinot, J. M., Tintoré, J., and Gomis, D.: Multivariate analysis of the surface circulation in  
 1508 the Balearic Sea, Prog. Oceanogr., 36, 343–376, [https://doi.org/10.1016/0079-](https://doi.org/10.1016/0079-6611(96)00003-1)  
 1509 6611(96)00003-1, 1995.

1510 Rayner, N. A., Parker, D. E., Horton, E. B., Folland, C. K., Alexander, L. V., Rowell, D.  
 1511 P., Kent, E. C., and Kaplan, A.: Global analyses of sea surface temperature, sea ice, and  
 1512 night marine air temperature since the late nineteenth century, J. Geophys. Res. Atmos.,  
 1513 108, <https://doi.org/10.1029/2002jd002670>, 2003.

1514 Renault, L., Oguz, T., Pascual, A., Vizoso, G., and Tintore, J.: Surface circulation in the  
 1515 Alboran Sea (western Mediterranean) inferred from remotely sensed data, *J. Geophys.*  
 1516 *Res. Ocean.*, 117, 1–11, <https://doi.org/10.1029/2011JC007659>, 2012.

1517 Richez, C., and Kergomard, C.: Characteristic features occurring in the Strait of Gibraltar  
 1518 as seen through remote sensing data, *Phys. Oceanogr. sea straits*, 441–455,  
 1519 [https://doi.org/10.1007/978-94-009-0677-8\\_21](https://doi.org/10.1007/978-94-009-0677-8_21), 1990.

1520 Rivaró, P., Messa, R., Massolo, S., and Frache, R.: Distributions of carbonate properties  
 1521 along the water column in the Mediterranean Sea: Spatial and temporal variations, *Mar.*  
 1522 *Chem.*, 121, 236–245, <https://doi.org/10.1016/j.marchem.2010.01.007>, 2010.

1523 Robinson, A. R., and Golnaraghi, M.: The physical and dynamical oceanography of the  
 1524 Mediterranean Sea, in: *Ocean Processes in Climate Dynamics: Global and Mediterranean*  
 1525 *Examples*, edited by: A. R. Robinson and K. Brink, 255–306, Dordrecht: Springer  
 1526 Netherlands, 1994.

1527 Robinson, A. R., Leslie, W. G., Theocharis, A., and Lascaratos, A.: Mediterranean Sea  
 1528 circulation, *Ocean Currents*, 1, 19, 2001.

1529 Rodgers, K. B., Schwinger, J., Fassbender, A. J., Landschützer, P., Yamaguchi, R.,  
 1530 Frenzel, H., Stein, K., Müller, J. D., Goris, N., Sharma, S., Bushinsky, S., Chau, T. T. T.,  
 1531 Gehlen, M., Gallego, M. A., Gloege, L., Gregor, L., Gruber, N., Hauck, J., Iida, Y., Ishii,  
 1532 M., Keppler, L., Kim, J. E., Schlunegger, S., Tjiputra, J., Toyama, K., Vaittinada Ayar,  
 1533 P., and Velo, A.: Seasonal Variability of the Surface Ocean Carbon Cycle: A Synthesis,  
 1534 *Global Biogeochem. Cycles*, 37, 1–34, <https://doi.org/10.1029/2023GB007798>, 2023.

1535 Sammari, C., Millot, C., and Prieur, L.: Aspects of the seasonal and mesoscale  
 1536 variabilities of the Northern Current in the western Mediterranean Sea inferred from the  
 1537 PROLIG-2 and PROS-6 experiments, *Deep-Sea Res. Part I*, 42, 893–917,  
 1538 [https://doi.org/10.1016/0967-0637\(95\)00031-Z](https://doi.org/10.1016/0967-0637(95)00031-Z), 1995.

1539 Sánchez-Garrido, J. C., García Lafuente, J., Álvarez Fanjul, E., Sotillo, M. G., and de los  
 1540 Santos, F. J.: What does cause the collapse of the western Alboran gyre? Results of an  
 1541 operational ocean model, *Prog. Oceanogr.*, 116, 142–153,  
 1542 <https://doi.org/10.1016/j.pocean.2013.07.002>, 2013.

1543 Sánchez-Garrido, J. C., and Nadal, I.: The Alboran Sea circulation and its biological  
1544 response: A review, *Front. Mar. Sci.*, 9, 1–15,  
1545 <https://doi.org/10.3389/fmars.2022.933390>, 2022.

1546 Sarmiento, J., and Gruber, N.: *Ocean Biogeochemical Dynamics*, Princeton Univ. Press,  
1547 Princeton, <https://doi.org/10.1515/9781400849079>, 2006.

1548 Schneider, A., Tanhua, T., Körtzinger, A., and Wallace, D. W. R.: High anthropogenic  
1549 carbon content in the eastern Mediterranean, *J. Geophys. Res. Ocean.*, 115, 1–11,  
1550 <https://doi.org/10.1029/2010JC006171>, 2010.

1551 Schneider, A., Wallace, D. W., and Körtzinger, A.: Alkalinity of the Mediterranean Sea,  
1552 *Geophys. Res. Lett.*, 34(15), <https://doi.org/10.1029/2006GL028842>. 2007.

1553 Schroeder, K., García-Lafuente, J., Josey, S. A., Artale, V., Nardelli, B. B., Carrillo, A.,  
1554 ... and Zodiatis, G.: Circulation of the Mediterranean Sea and its variability, in: *The*  
1555 *Climate of the Mediterranean Region*, edited by: M. D. Alpert and L. O. Reinhold, 187,  
1556 2012.

1557 Shadwick, E. H., Thomas, H., Comeau, A., Craig, S. E., Hunt, C. W., and Salisbury, J.  
1558 E.: Air-Sea CO<sub>2</sub> fluxes on the Scotian Shelf: Seasonal to multi-annual variability,  
1559 *Biogeosciences*, 7, 3851–3867, <https://doi.org/10.5194/bg-7-3851-2010>, 2010.

1560 Sharp, J. D., Pierrot, D., Humphreys, M. P., Epitalon, J.-M., Orr, J. C., Lewis, E. R., and  
1561 Wallace, D. W. R.: CO<sub>2</sub>SYSV3 for MATLAB (Version v3.2.1), Zenodo,  
1562 <https://doi.org/10.5281/zenodo.3950562>, 2023.

1563 Sisma-Ventura, G., Bialik, O. M., Yam, R., Herut, B., and Silverman, J.: pCO<sub>2</sub> variability  
1564 in the surface waters of the ultra-oligotrophic Levantine Sea: Exploring the air–sea CO<sub>2</sub>  
1565 fluxes in a fast warming region, *Mar. Chem.*, 196, 13–23,  
1566 <https://doi.org/10.1016/j.marchem.2017.06.006>, 2017.

1567 Smale, D. A., Wernberg, T., Oliver, E. C., Thomsen, M., Harvey, B. P., Straub, S. C., ...  
1568 and Moore, P. J.: Marine heatwaves threaten global biodiversity and the provision of  
1569 ecosystem services, *Nat. Clim. Change*, 9, 306–312, [https://doi.org/10.1038/s41558-019-](https://doi.org/10.1038/s41558-019-0364-4)  
1570 0364-4, 2019.

- 1571 Solé, J., Ballabrera-Poy, J., Macías, D., and Catalán, I. A.: The role of ocean velocity in  
1572 chlorophyll variability. A modelling study in the Alboran Sea, *Sci. Mar.*, 80, 249–256,  
1573 <https://doi.org/10.3989/scimar.04290.04A>, 2016.
- 1574 Speich, S., Madec, G., and Crépon, M.: A strait outflow circulation process study: The  
1575 case of the Alboran Sea, *J. Phys. Oceanogr.*, 26, 320–340, [https://doi.org/10.1175/1520-](https://doi.org/10.1175/1520-0485(1996)026<0320>2.0.CO;2)  
1576 0485(1996)026<0320>2.0.CO;2, 1996.
- 1577 Stanichny, S., Tigny, V., Stanichnaya, R., and Djenidi, S.: Wind driven upwelling along  
1578 the African coast of the Strait of Gibraltar, *Geophys. Res. Lett.*, 32, 1–4,  
1579 <https://doi.org/10.1029/2004GL021760>, 2005.
- 1580 Steinhoff, T. and Skjelvan, I.: Uncertainty analysis for calculations of the marine  
1581 carbonate system for ICOS-Oceans stations, ICOS OTC, [https://doi.org/10.18160/VB7C-](https://doi.org/10.18160/VB7C-Z758)  
1582 Z758, 2020.
- 1583 Taillandier, V., D’Ortenzio, F., and Antoine, D.: Carbon fluxes in the mixed layer of the  
1584 Mediterranean Sea in the 1980s and the 2000s, *Deep-Sea Res. Part I Oceanogr. Res. Pap.*,  
1585 65, 73–84, <https://doi.org/10.1016/j.dsr.2012.03.004>, 2012.
- 1586 Takahashi, T.: Global air-sea flux of CO<sub>2</sub> based on surface ocean pCO<sub>2</sub>, and seasonal  
1587 biological and temperature effects, *Deep-Sea Res. Part II*, 49, 1601–1622, 2002.
- 1588 Takahashi, T., Olafsson, J., Goddard, J. G., Chipman, D. W., and Sutherland, S. C.:  
1589 Seasonal variation of CO<sub>2</sub> and nutrients in the high-latitude surface oceans: A  
1590 comparative study, *Global Biogeochem. Cycles*, 7, 843–878,  
1591 <https://doi.org/10.1029/93GB02263>, 1993.
- 1592 Takahashi, T., Sutherland, S. C., Chipman, D. W., Goddard, J. G., Ho, C., Newberger,  
1593 T., and Munro, D. R.: Climatological distributions of pH, pCO<sub>2</sub>, total CO<sub>2</sub>, alkalinity, and  
1594 CaCO<sub>3</sub> saturation in the global surface ocean, and temporal changes at selected locations,  
1595 *Mar. Chem.*, 164, 95–125, <https://doi.org/10.1016/j.marchem.2014.06.004>. 2014.
- 1596 Takahashi, T., Sutherland, S. C., Sweeney, C., Poisson, A., Metzl, N., Tilbrook, B., Bates,  
1597 N., Wanninkhof, R., Feely, R. A., Sabine, C., Olafsson, J., and Nojiri, Y.: Global sea-air  
1598 CO<sub>2</sub> flux based on climatological surface ocean pCO<sub>2</sub>, and seasonal biological and

1599 temperature effects, *Deep-Sea Res. Part II Top. Stud. Oceanogr.*, 49, 1601–1622,  
1600 [https://doi.org/10.1016/S0967-0645\(02\)00003-6](https://doi.org/10.1016/S0967-0645(02)00003-6), 2002.

1601 Tanhua, T., Hainbucher, D., Schroeder, K., Cardin, V., Álvarez, M., and Civitarese, G.:  
1602 The Mediterranean Sea system: A review and an introduction to the special issue, *Ocean*  
1603 *Sci.*, 9, 789–803, <https://doi.org/10.5194/OS-9-789-2013>, 2013.

1604 Touratier, F., and Goyet, C.: Decadal evolution of anthropogenic CO<sub>2</sub> in the northwestern  
1605 Mediterranean Sea from the mid-1990s to the mid-2000s, *Deep-Sea Res. Part I Oceanogr.*  
1606 *Res. Pap.*, 56, 1708–1716, <https://doi.org/10.1016/J.DSR.2009.05.015>, 2009.

1607 Turi, G., Lachkar, Z., and Gruber, N.: Spatiotemporal variability and drivers of pCO<sub>2</sub> and  
1608 air-sea CO<sub>2</sub> fluxes in the California Current System: An eddy-resolving modeling study,  
1609 *Biogeosciences*, 11, 671–690, <https://doi.org/10.5194/BG-11-671-2014>, 2014.

1610 Turi, G., Lachkar, Z., Gruber, N., and Münnich, M.: Climatic modulation of recent trends  
1611 in ocean acidification in the California Current System, *Environ. Res. Lett.*, 11, 014007,  
1612 <https://doi.org/10.1088/1748-9326/11/1/014007>, 2016.

1613 Ulses, C., Estournel, C., Marsaleix, P., Soetaert, K., Fourier, M., Coppola, L., Lefèvre,  
1614 D., Touratier, F., Goyet, C., Guglielmi, V., Kessouri, F., Testor, P., and Durrieu De  
1615 Madron, X.: Seasonal dynamics and annual budget of dissolved inorganic carbon in the  
1616 northwestern Mediterranean deep-convection region, *Biogeosciences*, 20, 4683–4710,  
1617 <https://doi.org/10.5194/bg-20-4683-2023>, 2023.

1618 Van Heuven, S., Pierrot, D., Rae, J. W. B., Lewis, E., and Wallace, D. W. R.: MATLAB  
1619 Program Developed for CO<sub>2</sub> System Calculations, ORNL/CDIAC-105b, Carbon Dioxide  
1620 Information Analysis Center, Oak Ridge National Laboratory, U.S. Department of  
1621 Energy, Oak Ridge, Tennessee,  
1622 [https://doi.org/10.3334/CDIAC/otg.CO2SYS\\_MATLAB\\_v1.1](https://doi.org/10.3334/CDIAC/otg.CO2SYS_MATLAB_v1.1), 2011.

1623 Vargas-Yáez, M., Plaza, F., García-Lafuente, J., Sarhan, T., Vargas, J. M., and Vélez-  
1624 Belchi, P.: About the seasonal variability of the Alboran Sea circulation, *J. Mar. Syst.*,  
1625 35, 229–248, [https://doi.org/10.1016/S0924-7963\(02\)00128-8](https://doi.org/10.1016/S0924-7963(02)00128-8), 2002.



1626 Viúdez, A., Pinot, J. M., and Haney, R. L.: On the upper layer circulation in the Alboran  
 1627 Sea, *J. Geophys. Res. Ocean.*, 103, 21653–21666, <https://doi.org/10.1029/98JC01082>,  
 1628 1998.

1629 Wanninkhof, R.: Relationship between wind speed and gas exchange over the ocean  
 1630 revisited, *Limnol. Oceanogr. Methods*, 12, 351–362,  
 1631 <https://doi.org/10.4319/lom.2014.12.351>, 2014.

1632 Wanninkhof, R., Doney, S. C., Peng, T.-H., Bullister, J. L., Lee, K., and Feely, R. A.:  
 1633 Comparison of methods to determine the anthropogenic CO<sub>2</sub> invasion into the Atlantic  
 1634 Ocean, *Tellus B*, 51, 511–530, <https://doi.org/10.3402/tellusb.v51i2.16335>, 1999.

1635 Wanninkhof, R., Pierrot, D., Sullivan, K., Mears, P., and Barbero, L.: Comparison of  
 1636 discrete and underway CO<sub>2</sub> measurements: Inferences on the temperature dependence of  
 1637 the fugacity of CO<sub>2</sub> in seawater, *Mar. Chem.*, 247, 104178,  
 1638 <https://doi.org/10.1016/j.marchem.2022.104178>, 2022.

1639 Weiss, R.: Carbon dioxide in water and seawater: the solubility of a non-ideal gas, *Mar.*  
 1640 *Chem.*, 2(3), 203–215, [https://doi.org/10.1016/0304-4203\(74\)90015-2](https://doi.org/10.1016/0304-4203(74)90015-2). 1974.

1641 Whitehead, J. A., and Miller, A. R.: Laboratory simulation of the gyre in the Alboran Sea,  
 1642 *J. Geophys. Res. Ocean.*, 84, 3733–3742, <https://doi.org/10.1029/jc084ic07p03733>,  
 1643 1979.

1644 Wimart-Rousseau, C., Lajaunie-Salla, K., Marrec, P., Wagener, T., Raimbault, P.,  
 1645 Lagadec, V., Lafont, M., Garcia, N., Diaz, F., Pinazo, C., Yohia, C., Garcia, F., Xueref-  
 1646 Remy, I., Blanc, P. E., Armengaud, A., and Lefèvre, D.: Temporal variability of the  
 1647 carbonate system and air-sea CO<sub>2</sub> exchanges in a Mediterranean human-impacted coastal  
 1648 site, *Estuar. Coast. Shelf Sci.*, 236, <https://doi.org/10.1016/j.ecss.2020.106641>, 2020.

1649 Wimart-Rousseau, C., Wagener, T., Álvarez, M., Moutin, T., Fourrier, M., Coppola, L.,  
 1650 Niclas-Chirurgien, L., Raimbault, P., D’Ortenzio, F., Durrieu de Madron, X., Taillandier,  
 1651 V., Dumas, F., Conan, P., Pujo-Pay, M., and Lefèvre, D.: Seasonal and Interannual  
 1652 Variability of the CO<sub>2</sub> System in the Eastern Mediterranean Sea: A Case Study in the  
 1653 North Western Levantine Basin, *Front. Mar. Sci.*, 8, 1–18,  
 1654 <https://doi.org/10.3389/fmars.2021.649246>, 2021.

- 1655 Wimart-Rousseau, C., Wagener, T., Bosse, A., Raimbault, P., Coppola, L., Fourrier, M.,  
 1656 Ulses, C., and Lefèvre, D.: Assessing seasonal and interannual changes in carbonate  
 1657 chemistry across two time-series sites in the North Western Mediterranean Sea, *Front.*  
 1658 *Mar. Sci.*, 10, <https://doi.org/10.3389/fmars.2023.1281003>, 2023.
- 1659 Wolf-Gladrow, D. A., Zeebe, R. E., Klaas, C., Körtzinger, A., and Dickson, A. G.: Total  
 1660 alkalinity: The explicit conservative expression and its application to biogeochemical  
 1661 processes, *Mar. Chem.*, 106(1–2), 287–300,  
 1662 <https://doi.org/10.1016/j.marchem.2007.01.006>. 2007.
- 1663 Zambrano-Bigiarini, M., Majone, B., Bellin, A., Bovolo, C. I., Blenkinsop, S., and  
 1664 Fowler, H. J.: Hydrological impacts of climate change on the Ebro River basin, in: *The*  
 1665 *Ebro River Basin, The Handbook of Environmental Chemistry*, Springer, Berlin,  
 1666 Heidelberg. 13, 47–75, [https://doi.org/10.1007/698\\_2010\\_85](https://doi.org/10.1007/698_2010_85). 2010.
- 1667 Zarghamipour, M., Malakooti, H., and Bordbar, M. H.: Air–Sea CO<sub>2</sub> Exchange Over the  
 1668 Mediterranean Sea, the Red Sea and the Arabian Sea, *Int. J. Environ. Res.*, 18,  
 1669 <https://doi.org/10.1007/s41742-024-00586-6>, 2024.